

Optimization of Thermoelectric Properties of

Mg₃Sb_{2-x}Bi_x Phases

Optimization of Thermoelectric Properties of $\text{Mg}_3\text{Sb}_{2-x}\text{Bi}_x$ Phases

by

Trong Duc Phan

A thesis submitted to the School of Graduate Studies

In partial fulfillment of the requirements for the degree

MASTER OF SCIENCE

McMaster University

Hamilton, Ontario

2024

MASTER OF SCIENCE (2024)

Department of Chemistry and Chemical Biology

Title: Optimization of Thermoelectric Properties of $\text{Mg}_3\text{Sb}_{2-x}\text{Bi}_x$ Phases

Author: Trong Duc Phan

Supervisor: Professor Yuriy Mozharivskyj

NUMBER OF PAGES: xii, 51

Abstract

Thermoelectric (TE) materials can directly interconvert heat and electricity. Given escalating energy needs and greenhouse gas emissions, TE technology emerges as a promising green solution for recovering waste heat. Material performance is quantified by the dimensionless figure of merit ($ZT = S^2\sigma T/\kappa$), demanding a delicate balance of low thermal conductivity, high electrical conductivity, and high Seebeck coefficient. Unfortunately, optimizing these properties simultaneously proves challenging. Moreover, the widespread use of TE generators is hindered by their low efficiency, high cost, and environmental impact. This research seeks to develop cost-effective, abundant, non-toxic, and sustainable TE materials.

For an *n*-type material, this study explores the effects of Mg and Bi amounts, Mn doping, ball milling duration, and sintering conditions on the purity and thermoelectric properties of $\text{Mg}_3\text{Bi}_x\text{Sb}_{1.99-x}\text{Te}_{0.01}$. We found that excess Mg is necessary to achieve an *n*-type conduction even in the presence of Te, but too much Mg forms impurities that decrease thermoelectric efficiency. Additionally, Mg-rich annealing improves the material's grain size while preserving its *n*-type properties. Increasing Bi content leads to decreased phase stability and decomposition. Mn doping increases the carrier concentration and electrical conductivity but reduces the Seebeck coefficient. There is also an optimal ball milling time, beyond which decomposition of the material occurs. The highest figure of merit, zT of 1.55 was achieved for the $\text{Mg}_{3.27}\text{Mn}_{0.03}\text{Bi}_{1.3}\text{Sb}_{0.69}\text{Te}_{0.01}$ sample at 623K, which is comparable to the performance of Bi_2Te_3 .

In the second part, Ni was used to optimize carrier concentration by first replacing Mn in the Mg site, as in $\text{Mg}_{3.29}\text{Ni}_{0.01}\text{Bi}_{1.5}\text{Sb}_{0.49}\text{Te}_{0.01}$, and secondly, by acting as an independent dopant, as in $\text{Mg}_{3.27}\text{Mn}_{0.03}\text{Ni}_{0.01}\text{Bi}_{1.5}\text{Sb}_{0.49}\text{Te}_{0.01}$.

This resulted in an enhanced zT compared to Mn-doped samples, particularly at lower temperatures. *p*-Type samples were also fabricated and characterized. Their properties exhibited comparable performance to the reference data.

Acknowledgement

This master's degree is surely a meaningful achievement and experience in my life. I would like to appreciate all the support from professors, friends, and my family. I could not have fulfilled this without your help.

First of all, I would like to express my sincere appreciation to my supervisor Dr. Yuriy Mozharivskiy. Since the time of a research student in 2022, I have studied under his careful guidance for the last two years. I have learned great knowledge and researching experience which helped me make my first step on the research ladder.

I am also grateful to Dr. Yu-chih Tseng and CanmetMATERIALS, NRCan, for the research support. This support helped me to be concentrate on my studies.

Thankful gratitude goes out to Dr. Timothy Lo and Dr. Shaochang Song for their valuable advice and experiment supports, especially during my first year of the program. And finally, to everyone in our laboratory, it was wonderful working with all of you during the last two years.

I am grateful to my family, who have always stood beside me with emotional support. I am also grateful to my other Vietnamese friends who have supported me through a joyful community.

Thank you all for your encouragement!

List of Abbreviations

ω	Angular frequency
BM	Ball mill
k_B	Boltzmann constant
n	Carrier concentration
τ	Charge carrier relaxation time
e	Charge of carrier
Θ	Debye temperature
ρ_m	Density of the material
m^*	Effective mass
σ	Electrical conductivity
ρ	Electrical resistivity
EDS	Energy Dispersive Spectroscopy
$F\lambda(\eta)$	Generalized Fermi intergral over the energy range
C_v	Heat capacity
LF, LFA	Laser Flash Laser Flash Analysis
L	Lorenz number
μ	Mobility
Z	Number of valence electrons
λ_{ph}	Phonon mean free path
\hbar	Planck constant
V	Potential voltage
\dot{Q}	Rate of heat absorption

SEM	Scanning Electron Microscopy
α	Seebeck coefficient
v_s	Sound velocity
SPS	Spark Plasma Sintering
	Temperature
T, T_H, T_C	Temperature at hot side
	Temperature at cold side
	Thermal conductivity
$\kappa, \kappa_L, \kappa_e$	Lattice thermal conductivity
	Electronic thermal conductivity
zT	Thermoelectric material figure-of-merit
η	Thermoelectric efficiency
XRD, PXRD	X-ray diffraction Analysis
	Powder X-ray diffraction Analysis

Table of Contents

Abstract.....	iv
Acknowledgement	v
List of Abbreviations.....	vi
Table of Contents	viii
List of Figures and Tables.....	x
Chapter 1. Introduction	1
1.1 Energy Background	1
1.2 Thermoelectric Effect	2
1.2.1 Seebeck Effect	3
1.2.2 Peltier Effect	4
1.2.3 Thomson Effect and Thomson Relations.....	5
1.3 Thermoelectric Properties.....	6
1.3.1 Electrical Properties.....	6
1.3.2 Thermal Properties.....	7
1.3.3 Phonon Scattering.....	8
1.3.4 The Figure of Merit.....	10
1.3.5 Calculation of output power density and efficiency	11
Chapter 2. Experimental Methods	13
2.1 Synthesis	13
2.1.1 Ball Milling Method	13
2.1.2 Spark Plasma Sintering (SPS).....	14
2.2 Characterization Analysis	15
2.2.1 X-ray diffraction Analysis (XRD)	15

2.2.2 Scanning Electron Microscopy (SEM)	16
2.2.3 Energy Dispersive Spectroscopy (EDS)	17
2.3 Properties Measurement.....	18
2.3.1 Thermal Diffusivity.....	18
2.3.2 Electrical Resistance and Seebeck Coefficient	19
References.....	21
Chapter 3: Optimization of Thermoelectric Properties of n-type Mn- and Te-doped $Mg_3Sb_{2-x}Bi_x$ Phases.....	23
Abstract.....	23
Introduction.....	24
Experimental.....	26
Results and Discussion	27
Conclusion	35
References.....	36
Chapter 3: Supporting Information.....	41
Chapter 4: Thermoelectric Properties of n-type Ni-doped and p-type $Mg_3Sb_{2-x}Bi_x$ Phases	44
Introduction.....	44
Experimental.....	44
Results and Discussion for n-type Ni doped.....	45
Results and Discussion for p-type $Mg_3(Bi,Sb)_2$	48
References.....	50
Conclusions and Future Work.....	51

List of Figures and Tables

Figure and Table	Title	Page
Figure 1.1	Construction of thermoelectric module	2
Figure 1.2	Seebeck Effect	3
Figure 1.3	Peltier Effect	5
Figure 1.4	Carrier concentration dependence of Seebeck coefficient, electrical conductivity	10
Figure 1.5	The relation between efficiency and ZT with different temperature ranges	12
Figure 1.6	Power generation efficiency of different systems	12
Figure 2.1	Schematic diagram of the arc melting method ball milling method	13
Figure 2.2	Schematic diagram of the SPS method	14
Figure 2.3	Schematic diagram of XRD	15
Figure 2.4	Schematic diagram of the SEM	16
Figure 2.5	Schematic diagram of the EDS system	17
Figure 2.6	Schematic diagram of the laser flash system	18
Figure 2.7	Schematic diagram of the ZEM-3 system	19
Figure 3.1	Crystal structure of $\text{Mg}_3\text{Sb}_{2-x}\text{Bi}_x$ (space group $P\bar{3}m1$)	25
Figure 3.2	XRD patterns of $\text{Mg}_{2.97+y}\text{Mn}_{0.03}\text{Bi}_{1.5}\text{Sb}_{0.49}\text{Te}_{0.01}$ with different amount of extra Mg after ball milling (BM) and after SPS	28
Figure 3.3	XRD pattern of $\text{Mg}_{3.27}\text{Mn}_{0.03}\text{Bi}_1\text{Sb}_{0.99}\text{Te}_{0.01}$ for different ball milling duration	29
Figure 3.4	XRD pattern of the $\text{Mg}_{2.97}\text{Mn}_{0.03}\text{Bi}_{1.5}\text{Sb}_{0.49}\text{Te}_{0.01}$ SPS sample with and without annealing	30

Figure 3.5	XRD patterns of $\text{Mg}_{3.27}\text{Mn}_{0.03}\text{Bi}_x\text{Sb}_{1.99-x}\text{Te}_{0.01}$ after SPS with different Bi ratios	31
Figure 3.6	SEM/EDS analysis of the major phase in the SPS $\text{Mg}_{3.27}\text{Mn}_{0.03}\text{Bi}_1\text{Sb}_{0.99}\text{Te}_{0.01}$ sample	32
Figure 3.7	XRD patterns of $\text{Mg}_{3.27}\text{Mn}_{0.03}\text{Bi}_{1.5}\text{Sb}_{0.45}\text{Te}_{0.01}$ before and after ZEM-3 measurement	33
Figure 3.8	Electrical Properties of $\text{Mg}_{3.27}\text{Mn}_{0.03}\text{Bi}_x\text{Sb}_{1.99-x}\text{Te}_{0.01}$	34
Figure 3.9	Thermal Properties of $\text{Mg}_{3.27}\text{Mn}_{0.03}\text{Bi}_x\text{Sb}_{1.99-x}\text{Te}_{0.01}$	35
Figure 3.10	Comparison with Bi_2Te_3 other doped $\text{Mg}_3(\text{Bi,Sb})_2$ materials	35
Table 3.1	Density of $\text{Mg}_{3.27}\text{Mn}_{0.03}\text{Bi}_x\text{Sb}_{1.99-x}\text{Te}_{0.01}$ samples	27
Table 3.2	Unit cell parameters of the $\text{Mg}_{3.27}\text{Mn}_{0.03}\text{Bi}_x\text{Sb}_{1.99-x}\text{Te}_{0.01}$ samples	30
Figure S3.1	SEM/EDS analysis of the SPS $\text{Mg}_{3.27}\text{Mn}_{0.03}\text{Bi}_{1.3}\text{Sb}_{0.69}\text{Te}_{0.01}$ sample	41
Figure S3.2	SEM/EDS analysis of the SPS $\text{Mg}_{3.27}\text{Mn}_{0.03}\text{Bi}_{1.5}\text{Sb}_{0.49}\text{Te}_{0.01}$ sample	42
Figure S3.3	SEM/EDS analysis of the SPS $\text{Mg}_{3.27}\text{Mn}_{0.03}\text{Bi}_{1.7}\text{Sb}_{0.29}\text{Te}_{0.01}$ sample	43
Table S3.1	Atomic percent analysis of $\text{Mg}_{3.27}\text{Mn}_{0.03}\text{Bi}_{1.3}\text{Sb}_{0.69}\text{Te}_{0.01}$ sample	41
Table S3.2	Atomic percent analysis of $\text{Mg}_{3.27}\text{Mn}_{0.03}\text{Bi}_{1.5}\text{Sb}_{0.49}\text{Te}_{0.01}$ sample	42
Table S3.3	Atomic percent analysis of $\text{Mg}_{3.27}\text{Mn}_{0.03}\text{Bi}_{1.7}\text{Sb}_{0.29}\text{Te}_{0.01}$ sample	43
Figure 4.1	XRD patterns of $\text{Mg}_{3.29}\text{Ni}_{0.01}\text{Bi}_{1.5}\text{Sb}_{0.49}\text{Te}_{0.01}$ and $\text{Mg}_{3.27}\text{Mn}_{0.03}\text{Ni}_{0.01}\text{Bi}_{1.5}\text{Sb}_{0.49}\text{Te}_{0.01}$ after SPS	45
Figure 4.2	Electrical and Thermal Properties of $\text{Mg}_{3.29}\text{Ni}_{0.01}\text{Bi}_{1.5}\text{Sb}_{0.49}\text{Te}_{0.01}$ and $\text{Mg}_{3.27}\text{Mn}_{0.03}\text{Ni}_{0.01}\text{Bi}_{1.5}\text{Sb}_{0.49}\text{Te}_{0.01}$ in comparison with $\text{Mg}_{3.27}\text{Mn}_{0.03}\text{Bi}_{1.5}\text{Sb}_{0.49}\text{Te}_{0.01}$ and undoped $\text{Mg}_{3.3}\text{Bi}_{1.5}\text{Sb}_{0.5}$ sample	46

Figure 4.3 XRD patterns of $\text{Mg}_{3.15}\text{Bi}_1\text{Sb}_1$ and $\text{Mg}_{3.15}\text{Bi}_{1.5}\text{Sb}_{0.5}$ after ball mill (BM) and SPS 48

Figure 4.4 Electrical and Thermal Properties of $\text{Mg}_{3.15}\text{Bi}_1\text{Sb}_1$ and $\text{Mg}_{3.15}\text{Bi}_{1.5}\text{Sb}_{0.5}$ samples in comparison to the reference $\text{Mg}_3\text{Bi}_1\text{Sb}_1$ sample [4] 49

Chapter 1. Introduction

1.1 Energy Background

Energy demand and energy-related emissions have been among the greatest challenges of today. As fossil energy sources deplete, energy security is strongly dependent on transitioning to more sustainable solutions like renewable energy sources. However, it is crucial not only to find new energy sources but also to use existing ones efficiently and reduce emissions. It is estimated that approximately 60% of energy is wasted, primarily in the form of heat [1]. Thus, in addition to increasing efficiency, significant efforts have been invested in researching waste heat recycling. Among these efforts, thermoelectric technology has proven to be the most promising.

Thermoelectric modules can directly convert any heat gradient into electricity and vice versa. When one side of the module is hotter than the other, an electric potential develops. This potential increases as the temperature difference increases. Conversely, applying an electric current to the module creates a temperature difference, resulting in one hot side and one cold side. This principle enables both heating and cooling applications.

Thermoelectric modules are considered exceptionally reliable as they operate as solid-state energy converters without moving parts. Currently, thermoelectric modules find applications in temperature stabilization, cooling, power generation, heart pumping, and other areas [2]. However, their low efficiency compared to other power generators hinders widespread adoption [3]. Consequently, research into new materials and structures to enhance thermoelectric efficiency has gained significant attention. Moreover, the high cost and toxicity of current module materials necessitate the development of efficient, low-cost, non-toxic, and reliable thermoelectric materials.

For these reasons, this work investigates $\text{Mg}_3(\text{Bi,Sb})_2$ materials as an environmentally friendly alternative for thermoelectric modules. Both *n*-type and *p*-type materials were synthesized for this research, and both have demonstrated promising performance. Experimental synthesis and analysis were conducted to improve their properties by introducing dopants into the host matrix. The aim of this work is to optimize carrier concentration for achieving optimal performance.

1.2 Thermoelectric Effect

Thermoelectric materials exhibit two reversible energy conversion processes. The first effect is the Seebeck effect, where electricity is generated from a temperature gradient, and the second Peltier effect is the inverse. Discovered by Thomas J. Seebeck in 1823 and Jean C. Peltier in 1834, respectively [4], these phenomena have enabled the application of thermoelectric materials in numerous areas, notably waste heat recovery, thermal cooling, and power generation. Renowned for their solid-state mechanism, maintenance-free operation, and environmental friendliness [3], thermoelectric materials offer significant potential.

Fig. 1.1 shows a schematic view of a thermoelectric module.

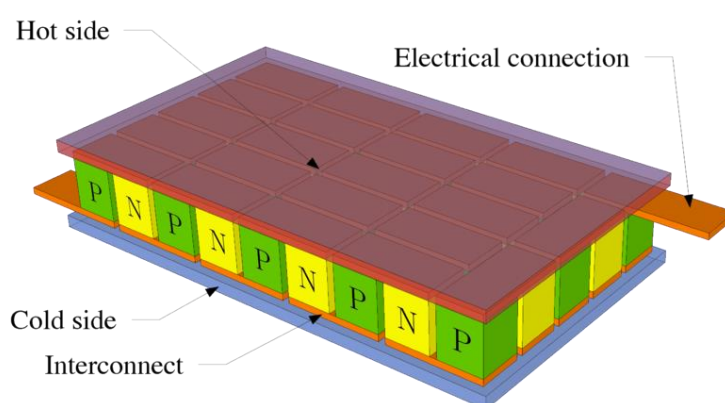


Figure 1.1 Construction of thermoelectric module [5]

A typical thermoelectric module consists of a pair of *p*-type and *n*-type legs connected electrically in series and thermally in parallel. One side of the module is designated as the hot

side, while the other is the cold side. A direct electric current is generated when a temperature difference exists between the two sides of the module. Conversely, applying a current to the module transfers heat to the hot side, thereby cooling the cold side. For near room temperature applications, p-type and n-type materials are primarily composed of bismuth (Bi) and tellurium (Te), achieving an energy conversion efficiency of approximately 5% [6]. The operating temperature range for typical modules is usually between 150 and 200 °C, although modules composed of other elements can function at 400 °C or higher. Moreover, different materials exhibit peak performance within specific temperature ranges. To optimize efficiency, two materials can be combined in a segmented module, with the high-temperature material in contact with the hot side and the other material in contact with the cold side [7].

1.2.1 Seebeck Effect

As mentioned, the thermoelectric effect is a general term encompassing two distinct effects: the Seebeck effect and the Peltier effect. The Seebeck effect involves the generation of electrical potential when a temperature gradient is applied to the module. This occurs because when heat is applied to one side (the hot side), electrons gain energy and migrate toward the cooler side, which has a lower energy level [4].

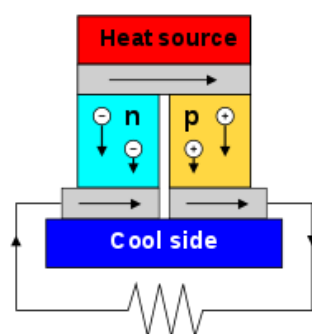


Figure 1.2 Seebeck Effect [18]

As the result, a voltage is observed between the two ends of a material when a temperature difference (ΔT) is applied. This is described by the equation:

$$V = \alpha\Delta T$$

where V is the potential voltage, α is the Seebeck coefficient, and ΔT is the temperature difference.

The Seebeck coefficient of a material quantifies the magnitude of the thermoelectric voltage generated in response to a temperature gradient. Since the absolute Seebeck coefficient is challenging to measure directly, relative values are typically determined. However, the absolute value can be calculated from the Thomson coefficient, which will be discussed later. Practically, the electric potential produced by the Seebeck effect is small, ranging from a few microvolts to millivolts. To increase voltage output, thermoelectric modules connect numerous couples in series. Despite this, applications for thermoelectric modules in large-scale electrical power generation remain limited [8].

1.2.2 Peltier Effect

The Peltier effect is the reverse process of the Seebeck effect, described by the following equation:

$$\dot{Q} = \pi I$$

where \dot{Q} is the rate of heat absorption/generation, π is the relative Peltier coefficient and I is the current.

From the equation, the heat absorption/generation rate is proportional to the current. Additionally, the heat and cold sides are reversed when the current is reversed. The sign of \dot{Q} depends on the direction of the current. Due to its ability to generate both hot and cold sides, the Peltier effect finds applications in both heat generation and refrigeration [9].

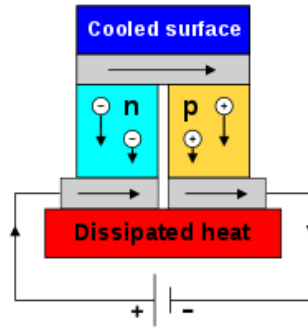


Figure 1.3 Peltier Effect [18]

1.2.3 Thomson Effect and Thomson Relations

The Thomson effect is an extension of the Seebeck-Peltier model used to derive absolute coefficients and their relationships. The equation for the Thomson effect is:

$$\dot{Q} = -\tau IVT$$

where τ is the Thomson coefficient [9].

Unlike the other two coefficients, the Thomson coefficient can be measured directly in an experiment. Thomson's relations describe the relationships among the three coefficients, derived from the first and second laws of thermodynamics, as shown in the following two equations:

$$\pi = \alpha T$$

$$\tau = T \frac{d\alpha}{dT}$$

From those two equations, the rate of heat absorption in Peltier cooling can be calculated as:

$$\dot{Q}_c = \alpha TI$$

1.3 Thermoelectric Properties

1.3.1 Electrical Properties

- Electrical conductivity

The electrical conductivity can be calculated from this equation:

$$\sigma = \frac{ne^2\tau}{m^*}$$

where n is the carrier concentration, e is the charge per carrier, τ is the charge mobility, and m^* is the effective electron mass [10].

According to Wiedemann-Franz law, the relationship of electrical conductivity to the thermal conductivity can be described in this equation:

$$\frac{\kappa_e}{\sigma} = LT$$

where κ_e is the electrical thermal conductivity and L is the Lorenz number, which is $L = 2.44 \times 10^{-8} \text{ W}\Omega\text{K}^{-2}$.

For metals, the carrier concentration, which is also the free electron concentration, can be calculated from the Drude model as:

$$n = \frac{N_A Z \rho_m}{m_a}$$

where N_A is the Avogadro constant, Z is the number of valence electrons, ρ_m is the density of the material, and m_a is the atomic mass [11].

- Seebeck coefficient

In metals, the Seebeck coefficient can be described with Mott formula as:

$$S = \frac{\pi^2 k_B^2 T}{3e} \frac{\partial E}{\partial E} \Big|_{E = E_F}$$

where k_B is the Boltzmann constant and e is the electrical conductivity [12].

1.3.2 Thermal Properties

The thermal conductivity in thermoelectric is the sum of electrical thermal conductivity κ_e and lattice thermal conductivity κ_l .

$$\kappa_{total} = \kappa_e + \kappa_l$$

While the electrical thermal conductivity dominates the total thermal conductivity in metal, the lattice thermal conductivity dominates in non-metal materials.

The electrical thermal conductivity can be calculated from Wiedemann-Franz Law:

$$\kappa_e = L\sigma T = ne\mu LT$$

where L is the Lorenz number $2.44 \times 10^{-8} W\Omega K^{-2}$ and σ is the electrical conductivity. The Lorenz number also can be calculated using a single parabolic band (SPB):

$$L = \frac{k^2 (1 + \lambda)(3 + \lambda)F_\lambda(\eta)F_{\lambda+2}(\eta) - (2 + \lambda)^2 F_{\lambda+1}(\eta)^2}{e^2 (1 + \lambda)^2 F_\lambda(\eta)}$$

where λ is a scattering exponent and $\lambda=0$ for acoustic phonon and alloying scattering, η is the relevant chemical potential depending on the carrier concentration, and $F_\lambda(\eta)$ is the generalized Fermi intergral over the entire energy range .

The lattice thermal conductivity can be calculated from:

$$\kappa_{lat} = \frac{1}{3} (C_v v_s \lambda_{ph}) = \frac{1}{3} C_v v^2 \tau$$

where C_v is the heat capacity, v_s is the sound velocity and λ_{ph} is the phonon mean free path and τ is the relaxation time. The phonon relaxation time is related to the mean free path through the phonon velocity. C_v can be described as:

$$C_V = 9Nk_B \left(\frac{T}{\theta}\right)^3 \int_0^{x_D} \frac{x^4 e^x}{(e^x - 1)^2} dx$$

where N is number of atoms, k_B is Boltzmann constant, and θ is the Debye temperature [13].

1.3.3 Phonon Scattering

Phonon scattering refers to the phenomenon where phonons are dispersed as they traverse a material. Several scattering mechanisms exist, including normal phonon-phonon scattering, Umklapp phonon-phonon scattering, phonon-boundary scattering, phonon-alloying scattering, and phonon-electron scattering. Each mechanism is characterized by a relaxation rate. According to Matthiessen's rule, the total inverse relaxation time equals the sum of the inverse relaxation rates for each scattering mechanism [14]. This can be expressed in the following equation:

$$\frac{1}{\tau_C} = \frac{1}{\tau_N} + \frac{1}{\tau_U} + \frac{1}{\tau_B} + \frac{1}{\tau_{PD}} + \frac{1}{\tau_e} + \dots$$

in which:

- Normal phonon-phonon scattering:

The general form of phonon-phonon scattering can be described as:

$$\frac{1}{\tau_N} = B\omega^a T^a$$

where B is the constant independent, ω is the angular frequency of the phonon and a is a dimensionless exponent that depends on the specific phonon scattering mechanism.

- Umklapp phonon-phonon scattering:

At the temperatures above the Debye temperature, Umklapp phonon-phonon scattering usually dominate the scattering effect. The Umklapp process occurs when two phonons collide, and a third phonon is created. The total crystal momentum changes by a reciprocal lattice vector.

- Boundary scattering:

Phonons scattering when travel through the boundaries of polycrystalline materials. This scattering mechanism is important for low-dimensional nanostructures

$$\frac{1}{\tau_B} = \frac{v}{L}$$

where v is the average group velocity of phonon and L is the grain length.

- Phonon alloying scattering:

The phonon alloying scattering is due to the lattice disorder in alloys which leads to point defect scattering. Scattering by point defect comes from both mass and strain contrast within the lattice. The scattering can be described as:

$$\frac{1}{\tau_{PD}} = \frac{V\omega^4}{4\pi v_p^2 v_g} \left(\sum_i f_i \left(1 - \frac{m_i}{\bar{m}}\right)^2 + \sum_i f_i \left(1 - \frac{r_i}{\bar{r}}\right)^2 \right)$$

where f_i is the fraction of atoms with mass m_i and radius r_i that consist of the average mass \bar{m} and radius \bar{r} respectively.

- Phonon-electron scattering:

Phonon-electron scattering occurs when the materials are heavily doped and can be described as:

$$\frac{1}{\tau_e} = \frac{E_{def}^2 m^{*2} \omega}{2\pi \hbar^3 d v_L}$$

where \hbar is the Planck constant, v_L is the longitudinal phonon velocity, m^* is the effective mass, E_{def} is the deformation potential, and d is the density.

1.3.4 The Figure of Merit

The performance of thermoelectric materials is measured by the dimensionless figure of merit zT :

$$zT = \frac{\alpha^2 \sigma}{\kappa} T$$

where α is Seebeck coefficient ($\mu\text{V/K}$), σ is electrical conductivity ($\mu\text{S/m}$), $\kappa = \kappa_e + \kappa_l$ is the sum of electrical and lattice thermal conductivity (W/mK), and T is the absolute temperature [6].

Higher zT materials exhibit enhanced energy conversion efficiency. To increase zT , it is essential to maximize the Seebeck coefficient and electrical conductivity while minimizing thermal conductivity. However, electrical conductivity and thermal conductivity are interrelated, as higher electrical conductivity contributes to increased electronic thermal conductivity (κ_e). Additionally, the Seebeck coefficient and electrical conductivity are interdependent on carrier concentration, as illustrated in the following figure:

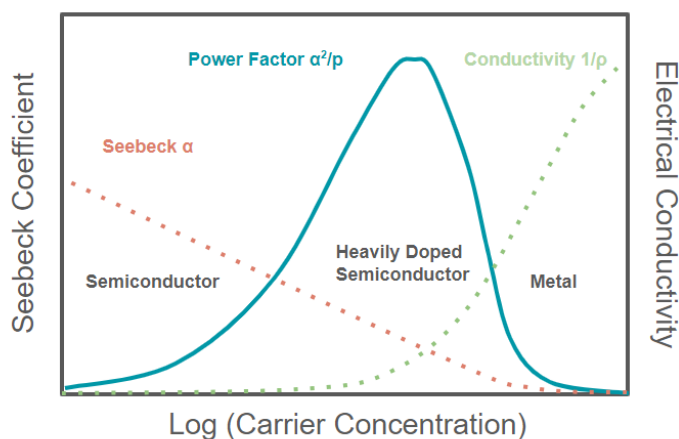


Figure 1.4 Carrier concentration dependence of Seebeck coefficient, electrical conductivity

From the figure, a higher carrier concentration leads to higher electrical conductivity but a lower Seebeck coefficient. Power factor is another crucial factor, calculated as the product of the Seebeck coefficient squared and electrical conductivity ($\text{PF} = \alpha^2 \sigma$). As shown in the

figure, the highest power factor typically occurs within the heavily doped semiconductor region, with carrier concentrations between 10^{19} and 10^{21} carriers per cm^3 . Therefore, optimizing carrier concentration is essential for improving zT . However, enhancing one property often compromises the other, making zT improvement a challenging task.

Since the discovery of the thermoelectric effect, achieving the efficiency necessary for large-scale application of thermoelectric modules has remained challenging. While high zT values exceeding 2.5 have been attained in some materials, these often suffer from high cost, toxicity, poor durability, and scalability issues. Consequently, commercial thermoelectric modules currently exhibit zT values around 1.

These materials can be categorized into three groups based on their operating temperature range: low-temperature materials, primarily bismuth (Bi) alloys with antimony (Sb), tellurium (Te), or selenium (Se); intermediate-temperature materials, such as lead (Pb)-based alloys; and high-temperature materials, like silicon-germanium (SiGe) alloys [16].

Beyond these conventional materials, promising new thermoelectric materials have emerged. Key criteria for these materials include a high-symmetry crystal structure promoting high band degeneracy, small electronegativity differences among constituent elements favouring covalent bonding, and a large complex unit cell with heavy atoms and strong anharmonicity to reduce intrinsic lattice thermal conductivity. To date, material families demonstrating some of these characteristics include SnSe, and half-Heusler compounds [6].

1.3.5 Calculation of output power density and efficiency

Like all heat engines, thermoelectric generators are bound by the Carnot limit on efficiency [17]:

$$\eta_{Carnot} = \frac{\Delta T}{T_H} = \frac{T_H - T_C}{T_H}$$

From the figure of merit, the maximum efficiency of a TE module can be calculated with this equation:

$$\eta_{max} = \frac{T_H - T_C}{T_H} \frac{\sqrt{1 + ZT} - 1}{\sqrt{1 + ZT} - \frac{T_C}{T_H}}$$

where T_H is the temperature at the hot side and T_C is the temperature on the cold side.

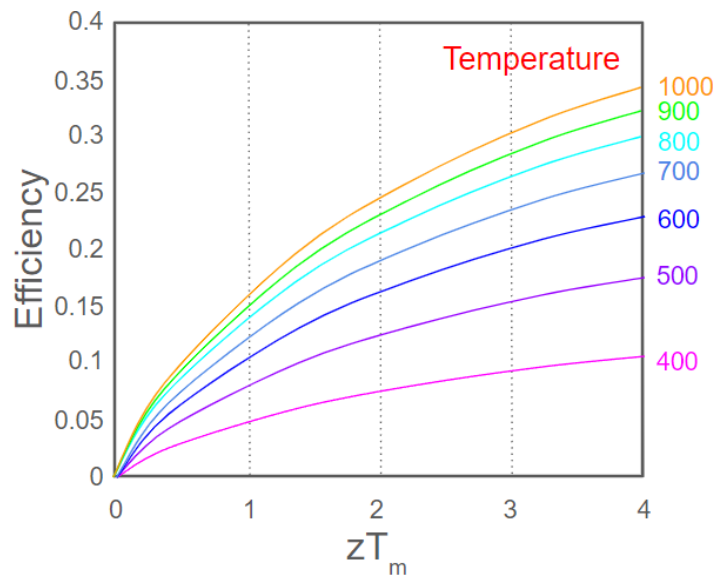


Figure 1.5 The relation between efficiency and zT with different T_1 (T_H) when $T_C=300K$.

From Figure 1.5, with a commercial zT of 1 and an operating temperature around 400 K ($T_C = 300K$), the efficiency of thermoelectric modules is approximately 5%. Compared to other power generators, thermoelectric module efficiency remains low. A zT of approximately 3 to 4 is required for thermoelectric generators to compete with other power generation systems [6].

Chapter 2. Experimental Methods

2.1 Synthesis

2.1.1 Ball Milling Method

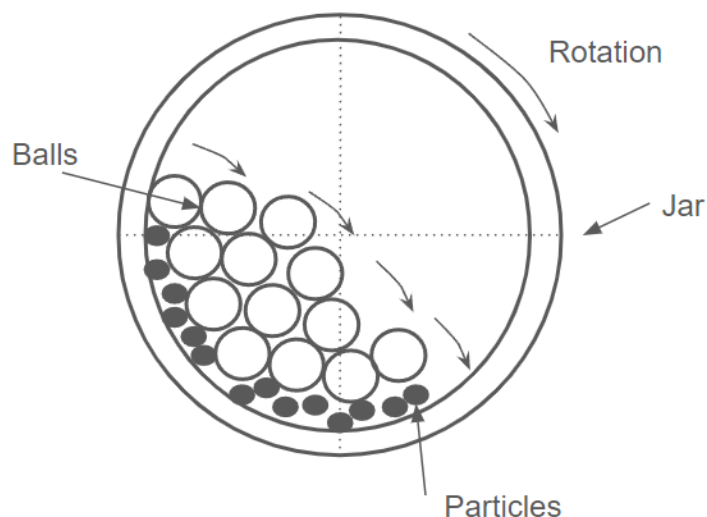


Figure 2.1 Schematic diagram of the arc melting method ball milling method

Ball milling is a versatile technique employed to reduce particle size and promote homogeneous mixing of materials. It involves the use of a cylindrical chamber containing grinding media, typically spherical balls, which are subjected to energetic collisions. Planetary ball mills, characterized by their complex orbital and rotational motion, are particularly effective in achieving fine particle sizes. During operation, the grinding media imparts high-energy impacts onto the material, leading to its fragmentation and dispersion.

Several factors influence the milling process, including ball-to-powder ratio, milling speed, and milling time. Additionally, the choice of grinding media material, such as steel, tungsten carbide, or zirconia, can impact the milling efficiency and product characteristics. To prevent contamination and enhance product purity, inert atmospheres or liquid media can be employed.

While ball milling offers advantages in terms of process simplicity and scalability, it also presents challenges. Excessive milling can induce defects or phase transformations in the material, and the process may be energy-intensive. Moreover, achieving uniform particle size distribution can be difficult, especially for hard or brittle materials [20].

2.1.2 Spark Plasma Sintering (SPS)

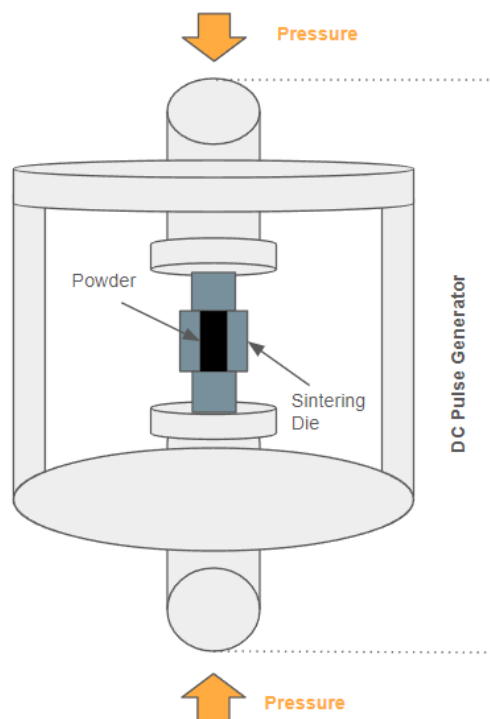


Figure 2.2 Schematic diagram of the SPS method

Spark plasma sintering (SPS) is an effective consolidation method for producing compact materials from powders. The initial powder is enclosed between two graphite punches within a graphite die. The entire assembly is then sintered by direct pulsed DC heating while simultaneously subjected to pressure at both ends.

SPS works by applying high pressure and pulsed electric current, it induces localized heating through spark generation between particles. This rapid heating, combined with pressure, promotes sintering, densification, and grain refinement. The process is notably faster and often requires lower temperatures than conventional sintering methods, enabling the

production of materials with enhanced properties [21]. Subsequent Joule heating enhances neck growth through diffusion. The softened particles undergo plastic deformation under uniaxial pressure [22].

Compared to other sintering methods, SPS offers advantages such as rapid heating and cooling rates, uniform heat distribution, and efficient power dissipation. These attributes contribute to shorter sintering times since the rapid heating can help to prevent excessive grain growth, as it reduces the time available for grain boundaries to migrate. However, limitations in sample size, complex shape formation, and equipment cost are drawbacks of the SPS method.

2.2 Characterization Analysis

2.2.1 X-ray diffraction Analysis (XRD)

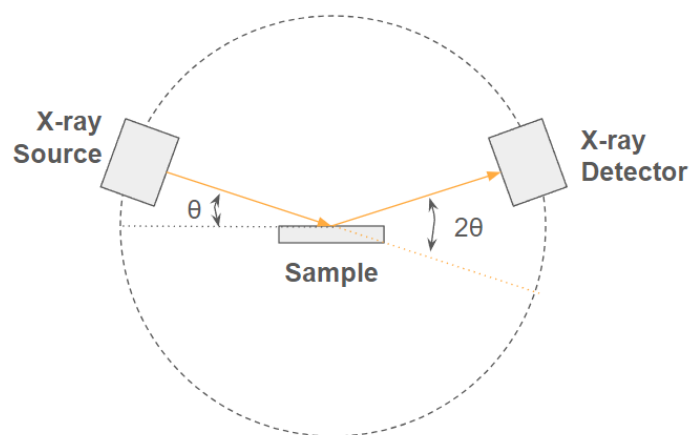
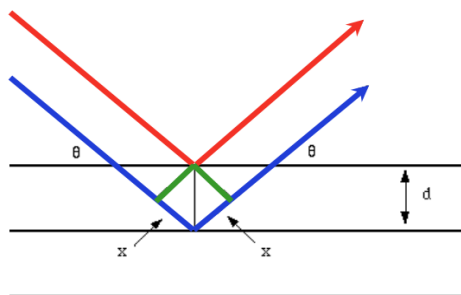


Figure 2.3 Schematic diagram of XRD

XRD is a well-known technique used for crystalline characterization, lattice constant determination, and purity measurement. It is one of the most powerful and rapid methods for these tasks, requiring minimal sample preparation. Essentially, XRD consists of three components: an X-ray tube, a sample holder, and an X-ray detector. X-rays are generated by a cathode ray tube, filtered to produce monochromatic radiation, collimated into a focused beam, and directed towards the sample [23].

The detection is based on the interference of X-rays and the sample. As the detector is rotated,



the intensity of the reflected X-rays is recorded, and the signals are converted into a count rate. The interaction of the incident rays with the sample produces constructive interference when conditions satisfy the Bragg's law [24]:

$$n\lambda = 2d \sin \theta$$

The XRD graphs display the intensity versus the angle of 2θ . In this work, the data is collected from the angle of 20° to 80° .

2.2.2 Scanning Electron Microscopy (SEM)

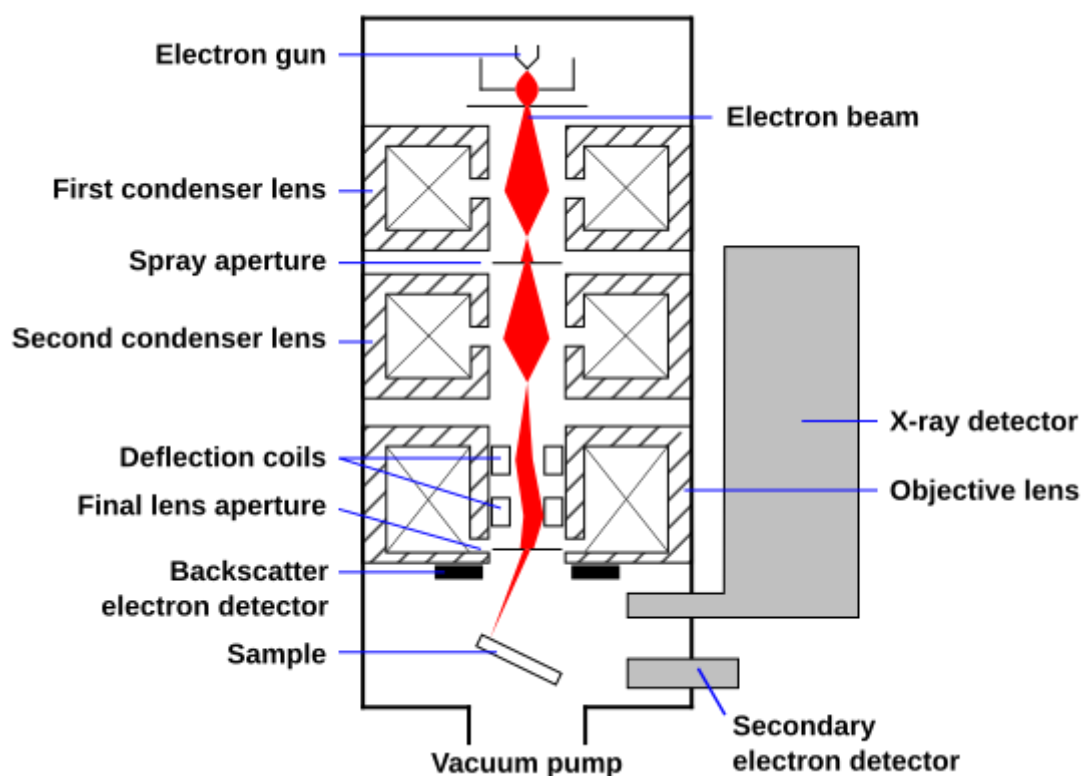


Figure 2.4 Schematic diagram of the SEM/EDS [25]

Scanning electron microscopy (SEM) is a widely used technique for examining and analyzing the microstructural characteristics of solid materials. An SEM system comprises an

electron source, electromagnetic lenses, an electron detector, a sample chamber, and a computer for data processing.

An electron gun emits a high-energy electron beam, which is then accelerated and focused by a lens system. Scanning coils positioned above the objective lens control the electron beam's position, enabling it to raster across the sample surface. Upon striking the sample, the electron beam generates various signals.

These signals provide information about morphology, composition, and structure. The kinetic energy of the incident electrons is dissipated, producing several types of signals, each applicable to specific analyses, such as SEM, energy-dispersive X-ray spectroscopy (EDS), and electron backscatter diffraction (EBSD). For SEM imaging, secondary electrons are employed to visualize sample morphology and topography [26].

2.2.3 Energy Dispersive Spectroscopy (EDS)

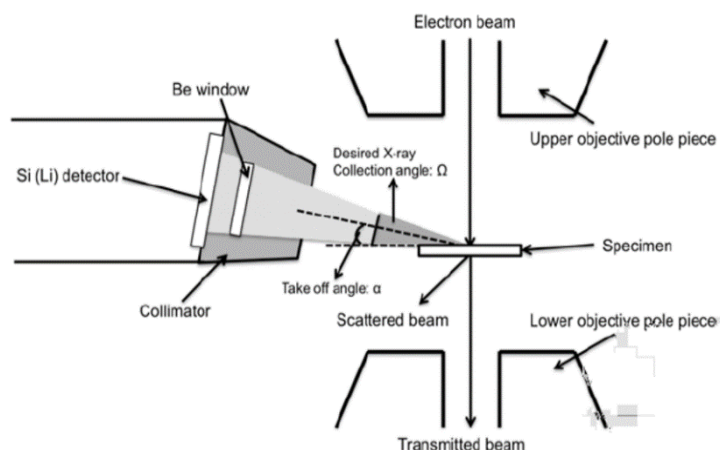


Figure 2.5 Schematic diagram of the EDS system [27]

Energy-dispersive X-ray spectroscopy (EDS) is a complementary technique commonly integrated with SEM for elemental analysis. The EDS system consists primarily of an X-ray detector, a liquid nitrogen cooling system, and data processing software. When the electron beam interacts with the sample, it generates X-rays characteristic of the elements present. The EDS detector captures these X-rays and converts their energy into electrical pulses.

The energy of these pulses is proportional to the energy of the incident X-rays, allowing for qualitative and quantitative elemental analysis. By analyzing the energy spectrum, the relative abundance of different elements can be determined. Advanced EDS systems can generate elemental maps, providing visual representations of elemental distribution within the sample.

Crucial to EDS performance is the detector's ability to accurately measure the energy of incoming X-rays. Factors such as detector efficiency, energy resolution, and peak-to-background ratio significantly influence the quality of the acquired data. To optimize performance, EDS systems often incorporate advanced signal processing algorithms and background subtraction techniques [27].

2.3 Properties Measurement

2.3.1 Thermal Diffusivity

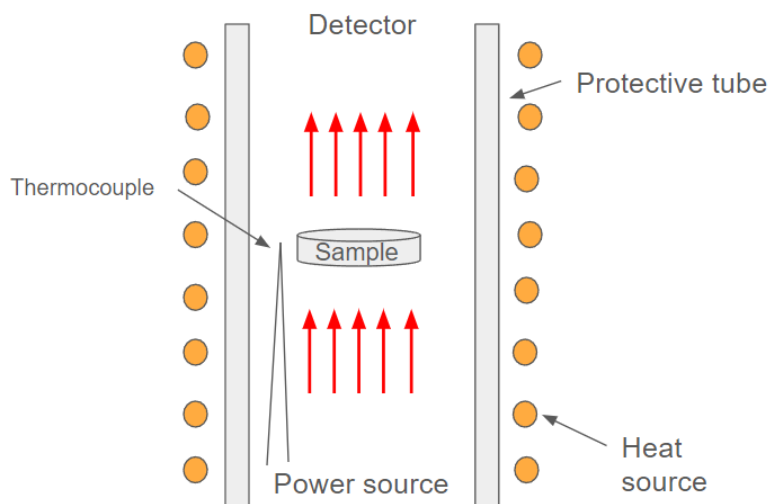


Figure 2.6 Schematic diagram of the laser flash system

Thermal diffusivity is measured using the Laser Flash (LF) method. This technique involves vertically positioning a sample within a furnace between a laser source and a sensor. A short-duration laser pulse is directed at the sample's rear surface, inducing a rapid

temperature rise. A detector positioned on the front surface measures the resulting time-dependent temperature increase. Thermal diffusivity is calculated based on this data using the following equation:

$$\alpha = 0.1388 \frac{d^2}{t_{1/2}}$$

where α is the thermal diffusivity, d is the thickness of the sample, and $t_{1/2}$ is the time to the half maximum [28].

The Laser Flash method necessitates a sample with flat, parallel top and bottom surfaces. Typically prepared as a disk or cube with a thickness ranging from 1 to 4 mm, the sample must be opaque, non-reflective, and exhibit good emission and absorption properties. To enhance these characteristics and prevent light reflection, samples often undergo a pre-treatment involving the application of a thin graphite coating [29].

The Laser Flash method offers several advantages, including simple sample preparation, straightforward operation, rapid measurement times, and the capability for high-temperature analysis. However, limitations include restrictions on sample size and complexity, and the strong dependence of accuracy on sample preparation and coating quality.

2.3.2 Electrical Resistance and Seebeck Coefficient

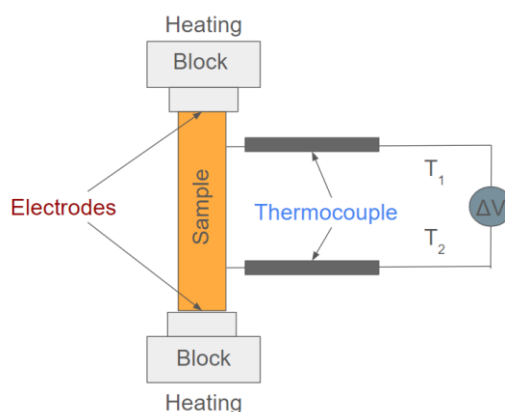


Figure 2.7 Schematic diagram of the ZEM-3 system

The ZEM-3 system enables simultaneous measurement of both electrical resistance and the Seebeck coefficient. It accommodates a wide range of materials, including semiconductors, oxides, and metals, in either bulk or thin-film form. The system's computer-controlled, automated operation ensures ease of use, high accuracy, and excellent repeatability [30].

- Electrical resistance is measured using the 4-point probe method. In the method, 4 probes (both ends and the thermocouple) are set up at almost identical intervals on the sample. Current is applied through both ends of the sample which creates a measurable voltage drop between the two legs of the thermocouple. The electrical resistivity then can be calculated using Ohm's law:

$$\rho = \frac{1}{\sigma} = \frac{A\Delta V}{I\Delta x}$$

where $\frac{\Delta V}{\Delta x}$ is the potential gradient in the direction of the current, A is the cross-sectional area and I is the current flowing through the sample.

- Seebeck coefficient is measured using a steady DC method. During the process, the bottom of the sample is heated by the lower block to create a temperature difference. Seebeck coefficient is calculated by measuring the upper and lower temperatures T_1 and T_2 , along with the measurement of thermal electromotive force between two probes, using this equation:

$$S = \frac{\Delta V}{T_1 - T_2}$$

The measurement is carried out with the temperature gradient of 20, 30, and 40°C between the upper block and lower block.

References

- [1] D. D. Chiras, *Environmental Science*, 2011.
- [2] D. Champier, "Thermoelectric generators: A review of applications," *Energy Conversion and Management*, vol. 140, pp. 167-181, 2017.
- [3] F. J. DiSalvo, "Thermoelectric Cooling and Power Generation," *Science*, vol. 285, pp. 703-706, 1999.
- [4] Dongliang Zhao, Gang Tan, "A review of thermoelectric cooling: Materials, modeling and applications," *Applied Thermal Engineering*, vol. 66, pp. 15-24, 2014.
- [5] Wikipedia. (2024). Retrieved from <https://en.wikipedia.org/wiki/Peltiereffect>
- [6] T. M. T. Jian He, "Advances in thermoelectric materials research: Looking back and moving forward," *Science*, vol. 357, 2017.
- [7] "Thermoelectric Engineering," [Online]. Available: <http://thermoelectrics.matsci.northwestern.edu/thermoelectrics/engineering.html>.
- [8] "Seebeck effect," [Online]. Available: <https://searchnetworking.techtarget.com/definition/Seebeck-effect>.
- [9] Gould, C.A.; Shamma, N.Y.A.; Grainger, S.; Taylor, I., "A comprehensive review of thermoelectric technology, micro-electrical and power generation properties".
- [10] Safa Kasap, Cyril Koughia, Harry E. Ruda, "Electrical Conduction in Metals and Semiconductors," in *Handbook of Electronic and Photonic Materials*, Springer.
- [11] M. Ashcroft, *Solid State Physics*, Cengage Learning, 1976.
- [12] I. Terasaki, "Introduction to Thermoelectricity".
- [13] David W. Hahn, M. Necati Özisik, in *Heat Conduction*, 2012.
- [14] J. M. Ziman, in *Electrons and Phonons: The Theory of Transport Phenomena in Solids*, 1960.
- [15] L. L. Baranowski, G. J. Snyder, Eric S. Toberer, "The Misconception of Maximum Power and Power Factor in Thermoelectrics," *J. Applied Physics*, vol. 115, 2013.
- [16] L.-D. Z. Yu Xiao, "Charge and phonon transport in PbTe-based thermoelectric materials," *Quantum Materials*, 2018.
- [17] Landau, L.D.; E.M. Lifshitz, *Electrodynamics of continuous media*, Pergamon Press, 1960.
- [18] Wikipedia. (2024). Retrieved from https://en.wikipedia.org/wiki/Thermoelectric_effect
- [20] W. Cao, "Synthesis of Nanomaterials by High Energy Ball Milling," Skyspring Nanomaterials, Inc..
- [21] T. K. M. Suárez, "Challenges and Opportunities for Spark Plasma Sintering: A Key Technology for a New Generation of Materials," in *Sintering Applications*, 2012.

- [22] O. Guillon et al., "Field-Assisted Sintering Technology/Spark Plasma Sintering: Mechanisms, Materials, and Technology Developments," *Advanced Engineering Materials*, 2014.
- [23] B. L. Dutrow, "Geochemical Instrumentation and Analysis, X-ray Powder Diffraction (XRD)," [Online].
- [24] H. P. Myers, in *Introductory Solid State Physics*, 2002.
- [25] Wikipedia. (2024). Retrieved from from https://en.wikipedia.org/wiki/Scanning_electron_microscope
- [26] "Nanoscience, Scanning Electron Microscopy" [Online]. Available: <https://www.nanoscience.com/techniques/scanning-electron-microscopy/>.
- [27] Ii S. Nanoscale Chemical Analysis in Various Interfaces with Energy Dispersive X-Ray Spectroscopy and Transmission Electron Microscopy [Internet]. X-Ray Spectroscopy. InTech; 2012. Available from: <http://dx.doi.org/10.5772/31645>
- [28] "Laser Flash Method " [Online]. Available: <https://thermtest.com/history-3-laser-flash-method>.
- [29] "When and How Must Samples Be Coated During LFA Measurements?," [Online]. Available: <https://www.netzsch-thermal-academy.com/en/e-learning/tips-tricks/when-and-how-must-samples-be-coated-during-lfa-measurements/>.
- [30] "ZEM-3 series," [Online]. Available: <https://showcase.ulvac.co.jp/en/products/heat-treatment-and-thermal-properties/thermoelectric-evaluation-device/thermoelectric-properties/zem-3series.html>.

Chapter 3: Optimization of Thermoelectric Properties of n-type Mn- and Te-doped $\text{Mg}_3\text{Sb}_{2-x}\text{Bi}_x$ Phases

This chapter is based on the manuscript of "Optimization of Thermoelectric Properties of n-type Mn- and Te-doped $\text{Mg}_3\text{Sb}_{2-x}\text{Bi}_x$ Phases" which was submitted to the Journal of Alloys and Compounds in August 2024. The research was carried out by the author. Dr Yuriy Mozharivskyj contributed to editing the text. Dr. Timothy Lo, Dr. Shaochang Song and Dr. Yu-Chih Tseng helped with some of the measurements.

Abstract

This study explores the effects of Mg and Bi amounts, ball milling duration, and sintering conditions on the purity and thermoelectric properties of the Mn- and Te-doped $\text{Mg}_3\text{Sb}_{2-x}\text{Bi}_x$ phases. We found that excess Mg is necessary to achieve an *n*-type conduction even in the presence of Te, but too much Mg forms impurities that decrease thermoelectric efficiency. Additionally, Mg-rich annealing improves the material's grain size while preserving its *n*-type properties. Increasing Bi content leads to lower phase stability and decomposition. Mn doping increases the carrier concentration and electrical conductivity but reduces the Seebeck coefficient. There is also an optimal ball milling time, beyond which decomposition of the material occurs. The highest figure of merit, *zT* of 1.55 was achieved for the $\text{Mg}_{3.27}\text{Mn}_{0.03}\text{Bi}_{1.30}\text{Sb}_{0.69}\text{Te}_{0.01}$ sample at 623K, which is comparable to the performance of Bi_2Te_3 . Our findings suggest that $\text{Mg}_3\text{Sb}_{2-x}\text{Bi}_x$ phases are promising low-cost and environmentally friendly thermoelectric materials for low to mid-range temperature applications.

Introduction

Thermoelectric materials can convert heat directly into electricity and can be employed for waste heat recovery. Thus, thermoelectric technology presents a captivating opportunity for energy conservation [1]. However, widespread adoption of thermoelectric technology is held back by energy conversion efficiency, which is tied to the material's dimensionless figure of merit, denoted as zT . The zT parameter is defined by the equation $zT = S^2\sigma T/(\kappa_l + \kappa_e)$, where S , σ , κ_l , κ_e , and T are the Seebeck coefficient, electrical conductivity, lattice thermal conductivity, electronic thermal conductivity, and absolute temperature, respectively [2]. High zT requires high electrical conductivity, high Seebeck coefficient, and low thermal conductivity. However, it is challenging to optimize these parameters simultaneously as they are interconnected [2,3].

Currently, most of the high performing thermoelectric materials achieve optimal zT values at high temperatures. Only a limited number of materials demonstrate good performance at or near room temperature, such as $(\text{Bi,Sb})_2(\text{Te,Se})_3$ [4], MgAgSb [5], and $\text{Mg}_3\text{Sb}_{2-x}\text{Bi}_x$ phases [6]. However, the widespread use of popular Bi_2Te_3 materials can be hindered by the low natural abundance of Te [7]. In this light, $\text{Mg}_3\text{Sb}_{2-x}\text{Bi}_x$ phases consisting of more abundant elements are more attractive. Mg_3Sb_2 and Mg_3Bi_2 were discovered in 1933 and adopt a trigonal anti $\alpha\text{-La}_2\text{O}_3$ structure with the space group $P\bar{3}m1$ [8]. The chemical composition of the $\alpha\text{-La}_2\text{O}_3$ structure can be written as AB_2C_2 . In case of $\text{Mg}_3\text{Sb}_{2-x}\text{Bi}_x$, both the A and B sites are occupied by Mg atoms denoted as Mg1 and Mg2. The Mg2 site is tetrahedrally coordinated with Sb/Bi and forms the B_2C_2 layer while the Mg1 site sits in octahedral voids between the layers [9,10].

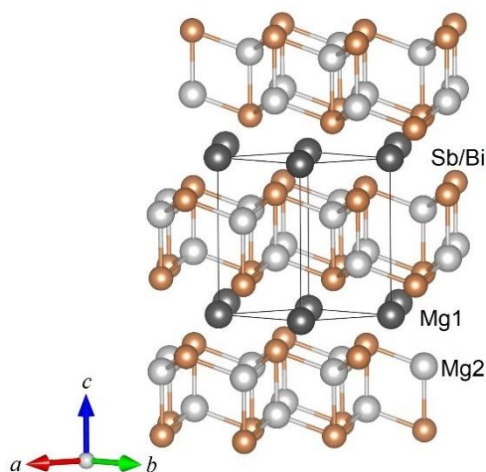


Figure 3.1. Crystal structure of $\text{Mg}_3\text{Sb}_{2-x}\text{Bi}_x$ (space group $P\bar{3}m1$).

When alloying with more electropositive alkaline earth metals (Ca, Sr, Ba) and lanthanides (La, Yb), the Mg1 site is preferentially occupied, while the Mg2 site is preferentially occupied by more electronegative metals such as Zn, Mn, and Cd [11,12].

Calculation shows that Mg_3Sb_2 is a semiconductor with a band gap of approximately 0.5 eV, whereas Mg_3Bi_2 is a semimetal [13–15]. By combining Sb and Bi, an optimal band gap can be achieved in $\text{Mg}_3\text{Mg}_3\text{Sb}_{2-x}\text{Bi}_x$, which enhances thermoelectric properties at specific temperatures [16,17]. The Bi/Sb alloying also reduces κ_1 by introducing strong point defect scattering of phonons [18]. $\text{Mg}_3\text{Sb}_{2-x}\text{Bi}_x$ shows persistent *p*-type behavior due to the formation of Mg vacancies [19,20]. However *p*-type $\text{Mg}_3\text{Sb}_{2-x}\text{Bi}_x$ shows a relative low performance with maximum *zT* of 0.6-0.7 at 750K [15,17,21]. In 2016, *n*-type $\text{Mg}_3\text{Sb}_{2-x}\text{Bi}_x$ was successfully synthesized with much higher performance compared to its *p*-type counterparts [22]. $\text{Mg}_{3.2}\text{Sb}_{1.5}\text{Bi}_{0.49}\text{Te}_{0.01}$ with excess Mg and Te doping on the Bi/Sb site has been reported to achieve a *zT* value of 1.5 at 723 K [22]. Mn and Nb doping on the Mg sites has been shown to improve the properties by manipulating the scattering mechanisms of low-temperature charge carriers [22–25]. In 2017, *zT* of 1.5 at 773K has been reported for $\text{Mg}_{3.05}\text{Nb}_{0.15}\text{Sb}_{1.5}\text{Bi}_{0.49}\text{Te}_{0.01}$ with an average *zT* \sim 0.87 (from 298K to 773K) [25]. In 2018, even higher *zT* of 1.85 at 723

K has been reported for $\text{Mg}_{3.15}\text{Mn}_{0.05}\text{Sb}_{1.5}\text{Bi}_{0.49}\text{Te}_{0.01}$ with an average $zT \sim 1.25$ (from 300 K to 723 K) [22,24].

In our study, we focused on Bi-rich compositions as Bi is less toxic than Sb [26]. Based on the previous results [22,24], we explored the $\text{Mg}_{2.97+y}\text{Mn}_{0.03}\text{Bi}_x\text{Sb}_{1.99-x}\text{Te}_{0.01}$ compositions ($x = 1, 1.3, 1.5, 1.7$ and $y = 0.1, 0.2, 0.3$). Extra Mg is crucial to achieve *n*-type properties during the synthesis. This is because some Mg is lost during the synthesis, due to its high vapor pressure [27], and an excess amount of Mg is required to compensate for these losses [28,29]. Additionally, all samples had to be annealed so that elemental Mg left during synthesis can diffuse back into the structure and ensure the desired *n*-type properties [30]. The current work summarizes the role of different variables on the stability, purity and properties of the $\text{Mg}_{2.97+y}\text{Mn}_{0.03}\text{Bi}_x\text{Sb}_{1.99-x}\text{Te}_{0.01}$ phases.

Experimental

Starting elements Mg (powder, 99 wt.%, Sigma-Aldrich), Bi (99.999 wt.%, Alfa Aesar), Sb (powder, 99.999 wt.%, 5N Plus), Te (99.999 wt.%, Alfa Aesar), and Mn (powder, 99.99 wt.%, Alfa Aesar) were weighed according to the $\text{Mg}_{2.97+y}\text{Mn}_{0.03}\text{Bi}_x\text{Sb}_{1.99-x}\text{Te}_{0.01}$ composition ($x = 1, 1.3, 1.5, 1.7$ and $y = 0.1, 0.2, 0.3$). Excess Mg is added to compensate for the loss of Mg during synthesis. The elements were loaded into a stainless-steel ball-milling jar inside a glove box in the argon atmosphere with oxygen levels below 0.1 ppm. The ball to sample weight ratio was 20:1. The jar was capped with an air-tight lid inside the glove box. The samples were then ball milled for 1 hour at 400 rpm using the planetary ball mill machine (Fritsch PULVERISETTE 6). The resulting powder was loaded into a 12.7mm graphite die inside the glovebox and sintered using spark plasma sintering (SPS, Dr. Sinter SPS 211) at 873K under a pressure of approximately 50 MPa for 5 minutes, and then annealed at 473K for 10 minutes.

The sample purity was analyzed on the powder X-ray diffractometer (PANalytical X'Pert, CuK α 1, X'Celerator detector). The microstructure and composition were analyzed on a scanning electron microscope (TESCAN VEGA) equipped with an energy dispersive spectrometer (EDS). The density of samples measured by dividing the mass by the volume (the volume is calculated from cylinder shape samples after SPS) is above the 92% of the theoretical density (Table 1).

Table 3.1. Density of Mg_{3.27}Mn_{0.03}Bi_xSb_{1.99-x}Te_{0.01} samples.

	Density (%)
x = 1	94.6
x = 1.3	94.2
x = 1.5	94.4
x = 1.7	92.4

The Seebeck coefficient and electrical resistivity were measured simultaneously on a ZEM-3 system (ULVAC-RIKO, Japan) in a helium atmosphere at 0.01 MPa. Thermal diffusivity was measured on disc-shaped samples under argon flow conditions using laser flash analysis (Netzsch LFA-457). The

thermal conductivity was calculated from $\kappa = D \cdot c_p \cdot \rho$, where D , c_p , and, ρ are the thermal diffusivity, specific heat capacity, and density, respectively [24].

Results and Discussion

Effect of Excess Mg

Excess Mg is required to achieve *n*-type conduction in Mg₃(Bi,Sb)₂ alloys. Extra Mg prevents the formation of Mg vacancies, which act as electron acceptors and would otherwise force the material to be *p*-type [28]. Beyond the minimum amount of excess Mg needed to achieve *n*-type conduction, additional Mg can be detrimental as it forms impurities that increase thermal conductivity and decrease thermoelectric efficiency [28].

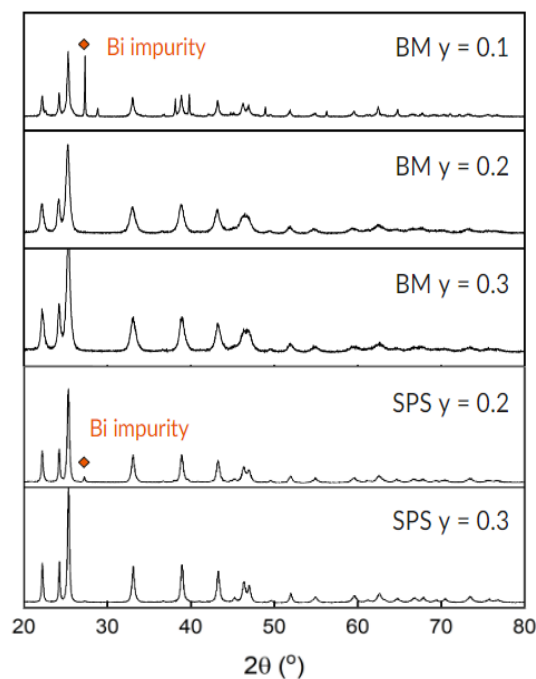


Figure 3.2. XRD patterns of $\text{Mg}_{2.97+y}\text{Mn}_{0.03}\text{Bi}_{1.5}\text{Sb}_{0.49}\text{Te}_{0.01}$ with different amount of extra Mg after ball milling (BM) and after SPS

The effect of extra Mg on the phase purity is demonstrated on the $\text{Mg}_{2.97+y}\text{Mn}_{0.03}\text{Bi}_{1.5}\text{Sb}_{0.49}\text{Te}_{0.01}$ samples. The initial addition of 0.1 Mg was insufficient to compensate for the Mg losses during the milling process, as the material still contained 10 at.% Bi and 3 at.% Sb impurities. When the amount of Mg was increased to 0.2, a pure phase was achieved after ball milling. However, this was not sufficient for the subsequent SPS process, as Bi impurity was still present after SPS. Finally, with the addition of 0.3 Mg, a pure $\text{Mg}_3(\text{Bi,Sb})_2$ -type phase was achieved after SPS. Based on these results, extra 0.3 Mg was used through the rest of this study.

Effect of Ball Milling Duration

The duration of ball milling also affects the phase purity. It was observed that a milling time of 1 hour is sufficient to obtain a phase-pure material (Figure 3.3). Increasing the milling time resulted in the decomposition of the sample, and emergence of Bi and Sb impurities. This

phenomenon can be explained by excessive fragmentation of particles, leading to the formation of defects and structural disorder during prolonged ball milling. Additionally, extreme local heating may occur, which may also affect the material stability [31,32].

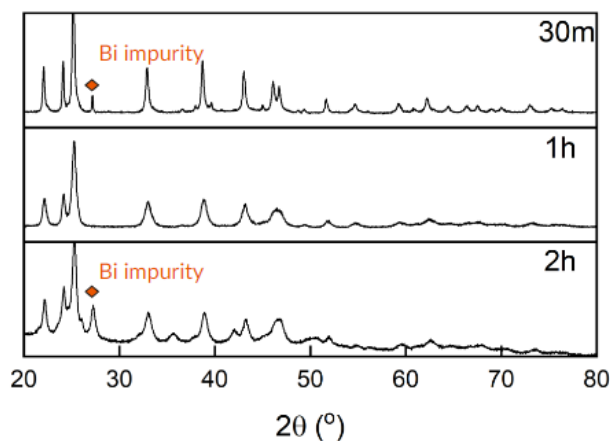


Figure 3.3. XRD pattern of $\text{Mg}_{3.27}\text{Mn}_{0.03}\text{Bi}_1\text{Sb}_{0.99}\text{Te}_{0.01}$ for different ball milling duration.

Effect of Annealing during SPS

During the spark plasma sintering, the samples are first held at 873 K and 50 MPa for 5 minutes, then cooled down to 473 K and held for 10 minutes with no pressure applied. At high temperatures, the samples partially decompose and release elemental Mg as an impurity [33]. Annealing the samples inside the SPS die at the lower temperature of 473K (below Bi melting point) allows for re-integration of Mg back into the structure. Such annealing in the presence of Mg vapor is known as Mg-rich annealing [30]. Figure 3.4 shows the effect of annealing on the $\text{Mg}_{2.97}\text{Mn}_{0.03}\text{Bi}_{1.5}\text{Sb}_{0.49}\text{Te}_{0.01}$ sample. The Bi impurity is very noticeable in the PXRD pattern without annealing, but it disappears after annealing.

Additionally, annealing increases the material's grain size which is beneficial for thermoelectric performance. Grain boundaries have a negative impact on the thermoelectric properties of $\text{Mg}_3(\text{Bi,Sb})_2$ at low temperatures [30]. Thus, low-temperature Mg-rich annealing permits grain growth and provides *n*-type behavior by keeping enough Mg in the structure [30].

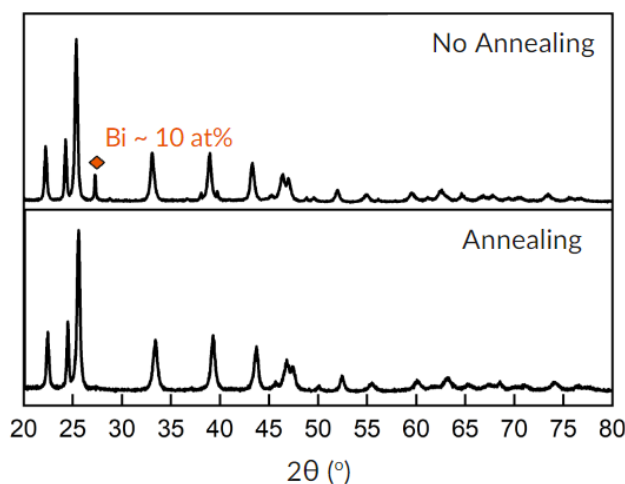


Figure 3.4. XRD pattern of the $\text{Mg}_{2.97}\text{Mn}_{0.03}\text{Bi}_{1.5}\text{Sb}_{0.49}\text{Te}_{0.01}$ SPS sample with and without annealing.

Different Bi Ratios

To evaluate the impact of Bi on the material's stability, the $\text{Mg}_{3.27}\text{Mn}_{0.03}\text{Bi}_x\text{Sb}_{1.99-x}\text{Te}_{0.01}$ samples with varying Bi amounts were prepared. Since Bi is larger than Sb ($r(\text{Bi}) = 143 \text{ pm}$ vs $r(\text{Sb}) = 133 \text{ pm}$) [34], increasing the Bi content leads to a larger unit cell (Table 2). Such expansion translates into longer bonds between Mg and Bi/Sb atoms, and consequently, the elastic modulus of the Bi-rich compounds becomes softer [35,36].

Table 3.2. Unit cell parameters of the $\text{Mg}_{3.27}\text{Mn}_{0.03}\text{Bi}_x\text{Sb}_{1.99-x}\text{Te}_{0.01}$ samples

Composition	a parameter (Å)	c parameter (Å)
x = 1	4.586(6)	7.285(1)
x = 1.3	4.608(5)	7.327(8)
x = 1.5	4.619(3)	7.343(3)
x = 1.7	4.623(2)	7.349(1)

More Bi also translates into lower structural stability, as manifested by higher amounts of elemental Bi in the Bi-rich samples after ball milling and SPS (Figure 3.5). Although indirectly, the charge transport properties, presented in the latter section, also point at the destabilizing effect of Bi. Specifically, the electrical conductivity starts to decrease sooner with increasing Bi content. This can be explained by the sample decomposition and formation of Bi and small amounts of Sb impurity, which are less conductive and also scatters the charge carriers.

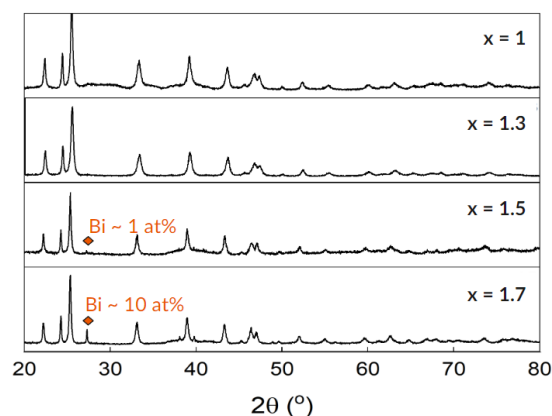


Figure 3.5. XRD patterns of $\text{Mg}_{3.27}\text{Mn}_{0.03}\text{Bi}_x\text{Sb}_{1.99-x}\text{Te}_{0.01}$ after SPS with different Bi ratios

SEM/EDS analysis

The $\text{Mg}_{2.97+y}\text{Mn}_{0.03}\text{Bi}_x\text{Sb}_{1.99-x}\text{Te}_{0.01}$ samples were analyzed using the SEM and EDS techniques. Herein, we focus on the $\text{Mg}_{3.27}\text{Mn}_{0.03}\text{Bi}_1\text{Sb}_{0.99}\text{Te}_{0.01}$ sample. Analysis for other 3 samples ($x = 1.3, 1.5$ and 1.7) is provided in the Supporting Information. The primary observation is the successful synthesis of the desired material. The $\text{Mg}_{3.27}\text{Mn}_{0.03}\text{Bi}_1\text{Sb}_{0.99}\text{Te}_{0.01}$ also contains the Mn impurity, which was at a lower level for $x = 1.3$ and could not be observed for $x = 1.5$ and 1.7 . These findings suggest that the synthesis parameters may need to be optimized to achieve a higher degree of Mn incorporation into some phases.

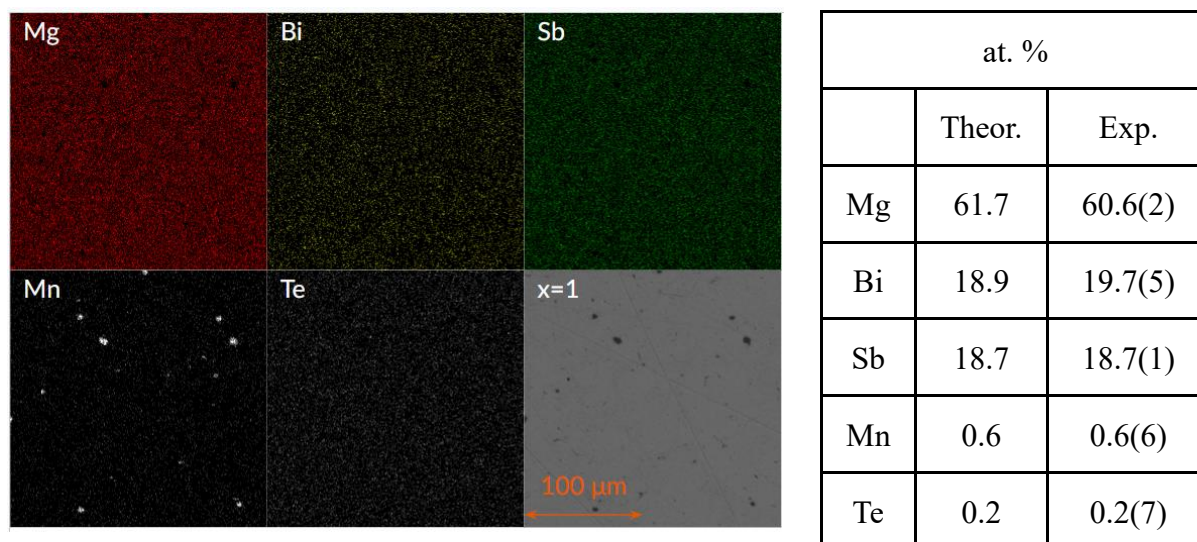


Figure 3.6. SEM/EDS analysis of the major phase in the SPS $\text{Mg}_{3.27}\text{Mn}_{0.03}\text{Bi}_x\text{Sb}_{1.99-x}\text{Te}_{0.01}$ sample.

Properties

The thermoelectric properties of the $\text{Mg}_{3.27}\text{Mn}_{0.03}\text{Bi}_x\text{Sb}_{1.99-x}\text{Te}_{0.01}$ samples are shown in Figures 3.8 and 3.9. As the Bi amount increases from $x = 1$ to 1.5, electrical resistivity and thermopower decreases, and the power factor increases, which can be attributed to the increased carrier concentration. The properties of the sample with $x = 1.7$ do not follow the same trend, which is likely due to larger presence of impurities. As the Bi content rises, the minima present in the charge transport and thermal properties shifts to lower temperatures as seen in Figures 3.8 and 3.9. This can be explained by the decomposition happening during the measurements. A higher amount of the Bi impurity in the $\text{Mg}_{3.27}\text{Mn}_{0.03}\text{Bi}_{1.5}\text{Sb}_{0.45}\text{Te}_{0.01}$ sample after thermoelectric measurements (Figure 3.7) supports this argument.

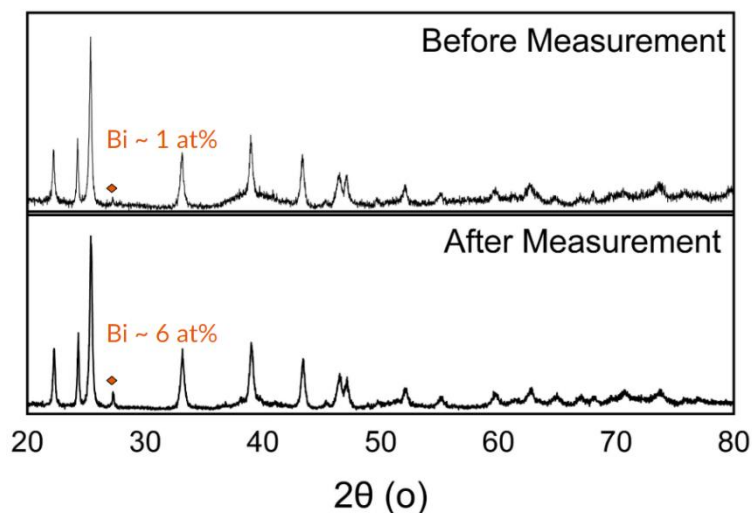
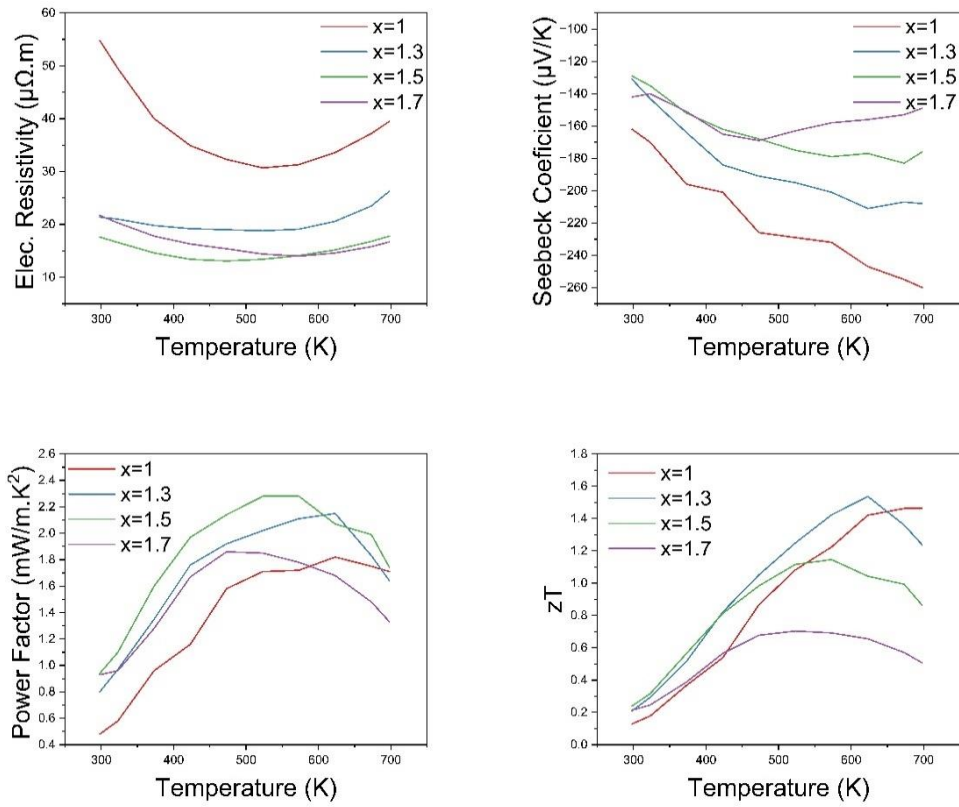
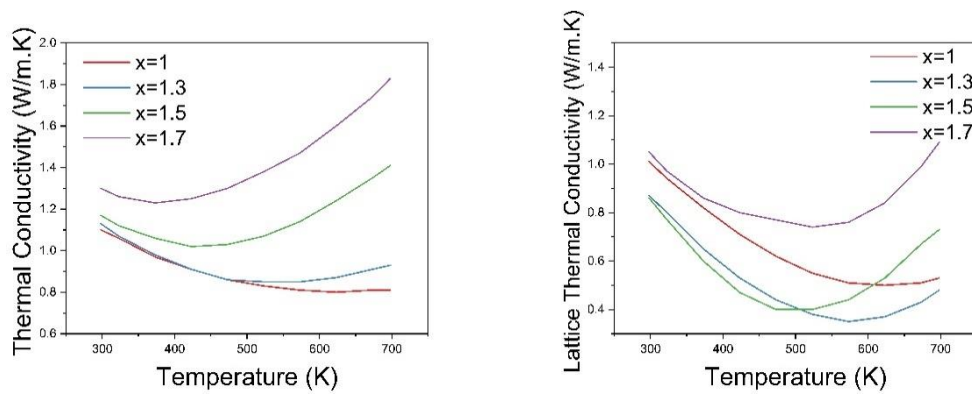


Figure 3.7. XRD patterns of $\text{Mg}_{3.27}\text{Mn}_{0.03}\text{Bi}_{1.5}\text{Sb}_{0.45}\text{Te}_{0.01}$ before and after ZEM-3 measurement.

Based on the minima in electrical resistivity, the decomposition temperature decreases from 623 K for $x = 1$ and $x = 1.3$ to 550 K for $x = 1.5$ and 480 K for $x = 1.7$. Decomposition leads to a significant increase in thermal conductivity at elevated temperatures, which can be attributed to a high thermal conductivity of elemental Bi and Sb ($k_{\text{Bi}} = 8 \text{ W/m}\cdot\text{K}$ and $k_{\text{Sb}} = 24 \text{ W/m}\cdot\text{K}$ at 273 K [34]).

The figure of merit, zT , for all studied samples is plotted in Figure 3.8 and for the $\text{Mg}_{3.27}\text{Mn}_{0.03}\text{Bi}_{1.30}\text{Sb}_{0.66}\text{Te}_{0.01}$ sample ($x = 1.30$) in Figure 3.10. The zT value for $\text{Mg}_{3.27}\text{Mn}_{0.03}\text{Bi}_{1.30}\text{Sb}_{0.66}\text{Te}_{0.01}$ peaks at 1.55 at 623K. This value is competitive with that of the Bi_2Te_3 material. For comparison, the literature data for $\text{Mg}_{3.05}\text{Sb}_{0.6}\text{Bi}_{1.4}\text{Te}_{0.01}$ [16] and $\text{Mg}_{3.175}\text{Mn}_{0.025}\text{Sb}_{1.5}\text{Bi}_{0.49}\text{Te}_{0.01}$ [24] are also plotted. The $\text{Mg}_{3.27}\text{Mn}_{0.03}\text{Bi}_{1.30}\text{Sb}_{0.66}\text{Te}_{0.01}$ sample shows slightly lower performance than $\text{Mg}_{3.175}\text{Mn}_{0.025}\text{Sb}_{1.5}\text{Bi}_{0.49}\text{Te}_{0.01}$.

Figure 3.8. Electrical Properties of $\text{Mg}_{3.27}\text{Mn}_{0.03}\text{Bi}_x\text{Sb}_{1.99-x}\text{Te}_{0.01}$ Figure 3.9. Thermal Properties of $\text{Mg}_{3.27}\text{Mn}_{0.03}\text{Bi}_x\text{Sb}_{1.99-x}\text{Te}_{0.01}$

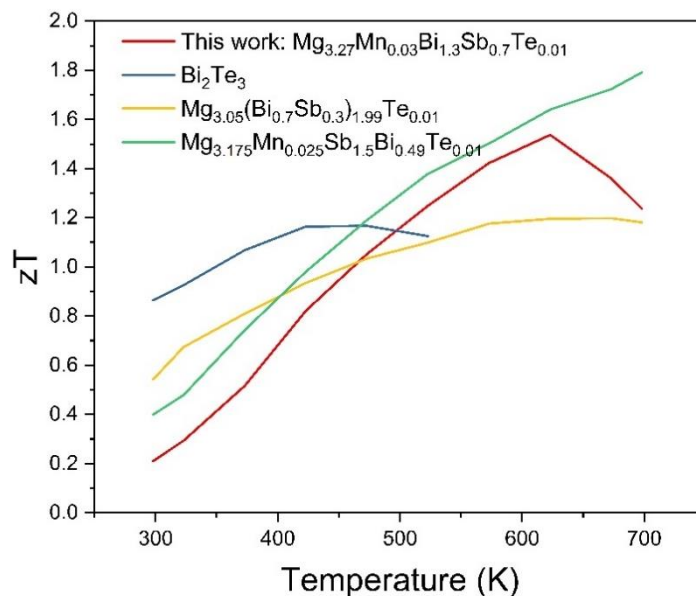


Figure 3.10. Comparison with Bi_2Te_3 other doped $Mg_3(Bi,Sb)_2$ materials.

(Bi_2Te_3 [36], $Mg_{3.05}(Bi_{0.7}Sb_{0.3})_{1.99}Te_{0.01}$ [16], $Mg_{3.175}Mn_{0.025}Sb_{1.5}Bi_{0.49}Te_{0.01}$ [24]).

Conclusion

Current studies highlighted the importance of extra Mg, proper balling time, and thermal annealing to produce $Mg_{3.27}Mn_{0.03}Bi_xSb_{1.99-x}Te_{0.01}$ samples with suitable thermoelectric properties. It was observed that while Bi addition improves the material performance, it also compromises its stability, leading to lower decomposition temperatures. The achieved zT values suggest that $Mg_{3.27}Mn_{0.03}Bi_xSb_{1.99-x}Te_{0.01}$ samples can be suitable for low to mid-range temperature applications. The peak zT value of 1.55 for $x = 1.3$ at 623 K makes this material competitive with Bi_2Te_3 at mid-range temperatures. If thermal stability of the $Mg_{3.27}Mn_{0.03}Bi_xSb_{1.99-x}Te_{0.01}$ materials could be improved, their low cost, environmental friendliness, and comparable performance can position them as a potential replacement for Bi_2Te_3 .

References

1. Bell LE. Cooling, heating, generating power, and recovering waste heat with thermoelectric systems. *Science*. 2008;321: 1457–1461. doi:10.1126/science.1158899
2. Snyder GJ, Toberer ES. Complex thermoelectric materials. *Nat Mater*. 2008;7: 105–114. doi:10.1038/nmat2090
3. He J, Tritt TM. Advances in thermoelectric materials research: Looking back and moving forward. *Science*. 2017;357. doi:10.1126/science.aak9997
4. Heremans JP, Cava RJ, Samarth N. Tetradymites as thermoelectrics and topological insulators. *Nat Rev Mater*. 2017;2: 17049. doi:10.1038/natrevmats.2017.49
5. Zhao H, Sui J, Tang Z, Lan Y, Jie Q, Kraemer D, et al. High thermoelectric performance of MgAgSb-based materials. *Nano Energy*. 2014;7: 97–103. doi:10.1016/j.nanoen.2014.04.012
6. Shu R, Zhou Y, Wang Q, Han Z, Zhu Y, Liu Y, et al. Mg₃₊ Sb Bi₂₋ Family: A Promising Substitute for the State-of-the-Art n-Type Thermoelectric Materials near Room Temperature. *Adv Funct Mater*. 2018; 1807235. doi:10.1002/adfm.201807235
7. Ying P, He R, Mao J, Zhang Q, Reith H, Sui J, et al. Towards tellurium-free thermoelectric modules for power generation from low-grade heat. *Nat Commun*. 2021;12: 1121. doi:10.1038/s41467-021-21391-1
8. Zintl E, Husemann E. Bindungsart und Gitterbau binärer Magnesiumverbindungen. *Zeitschrift für Physikalische Chemie*. 1933;21B: 138–155. doi:10.1515/zpch-1933-2112
9. Martinez-Ripoll M, Haase A, Brauer G. The crystal structure of α -Mg₃ Sb₂. *Acta Crystallogr B Struct Sci*. 1974;30: 2006–2009. doi:10.1107/S0567740874006285

10. Ahmadpour F, Kolodiazhnyi T, Mozharivskyj Y. Structural and physical properties of $Mg_{3-x}Zn_xSb_2$ ($x=0-1.34$). *J Solid State Chem.* 2007;180: 2420–2428. doi:10.1016/j.jssc.2007.06.011
11. Sun J, Singh DJ. Thermoelectric properties of AMg_2X_2 , AZn_2Sb_2 ($A = Ca, Sr, Ba$; $X = Sb, Bi$), and Ba_2ZnX_2 ($X = Sb, Bi$) Zintl compounds. *J Mater Chem A.* 2017;5: 8499–8509. doi:10.1039/C6TA11234J
12. Xia S, Myers C, Bobev S. Combined experimental and density functional theory studies on the crystal structures and magnetic properties of $Mg(Mg_{1-x}Mn_x)_2Sb_2$ ($x \approx 0.25$) and $BaMn_2Sb_2$. *Eur J Inorg Chem.* 2008;2008: 4262–4269. doi:10.1002/ejic.200800572
13. Kajikawa T, Kimura N, Yokoyama T. Thermoelectric properties of intermetallic compounds: $Mg_{3/2}Bi_2$ and $Mg_{3/2}Sb_2$ for medium temperature range thermoelectric elements. *Proceedings ICT'03 22nd International Conference on Thermoelectrics (IEEE Cat No03TH8726)*. IEEE; 2003. pp. 305–308. doi:10.1109/ICT.2003.1287510
14. Ponnambalam V, Morelli DT. On the thermoelectric properties of zintl compounds $Mg_3Bi_{2-x}Pn_x$ ($Pn = p$ and sb). *Journal of Elec Materi.* 2013;42: 1307–1312. doi:10.1007/s11664-012-2417-7
15. Condron CL, Kauzlarich SM, Gascoin F, Snyder GJ. Thermoelectric properties and microstructure of Mg_3Sb_2 . *J Solid State Chem.* 2006;179: 2252–2257. doi:10.1016/j.jssc.2006.01.034
16. Imasato K, Kang SD, Snyder GJ. Exceptional thermoelectric performance in $Mg_3Sb_{0.6}Bi_{1.4}$ for low-grade waste heat recovery. *Energy Environ Sci.* 2019;12: 965–971. doi:10.1039/C8EE03374A

1. 17. Xin HX, Qin XY. Electrical and thermoelectric properties of nanocrystal substitutional semiconductor alloys $\text{Mg}_3(\text{Bi Sb}_{1-x})_2$ prepared by mechanical alloying. *J Phys D Appl Phys.* 2006;39: 5331–5337. doi:10.1088/0022-3727/39/24/035
17. Gurunathan R, Hanus R, Dylla M, Katre A, Snyder GJ. Analytical Models of Phonon–Point-Defect Scattering. *Phys Rev Appl.* 2020;13: 034011. doi:10.1103/PhysRevApplied.13.034011
18. Nayeb-Hashemi AA, Clark JB. The Bi-Mg (Bismuth-Magnesium) system. *Bulletin of Alloy Phase Diagrams.* 1985;6: 528–533. doi:10.1007/BF02887150
19. Okamoto H. Mg-Sb (Magnesium-Antimony). *J Phs Eqil and Diff.* 2010;31: 574–574. doi:10.1007/s11669-010-9784-7
20. Bhardwaj A, Rajput A, Shukla AK, Pulikkotil JJ, Srivastava AK, Dhar A, et al. Mg_3Sb_2 -based Zintl compound: a non-toxic, inexpensive and abundant thermoelectric material for power generation. *RSC Adv.* 2013;3: 8504. doi:10.1039/c3ra40457a
21. Tamaki H, Sato HK, Kanno T. Isotropic Conduction Network and Defect Chemistry in $\text{Mg}_{3+\delta}\text{Sb}_2$ -Based Layered Zintl Compounds with High Thermoelectric Performance. *Adv Mater.* 2016;28: 10182–10187. doi:10.1002/adma.201603955
22. Kim S, Kim C, Hong Y-K, Onimaru T, Suekuni K, Takabatake T, et al. Thermoelectric properties of Mn-doped Mg–Sb single crystals. *J Mater Chem A.* 2014;2: 12311–12316. doi:10.1039/C4TA02386B
23. Chen X, Wu H, Cui J, Xiao Y, Zhang Y, He J, et al. Extraordinary thermoelectric performance in n-type manganese doped Mg_3Sb_2 Zintl: High band degeneracy, tuned carrier scattering mechanism and hierarchical microstructure. *Nano Energy.* 2018;52: 246–255. doi:10.1016/j.nanoen.2018.07.059

24. Shuai J, Mao J, Song S, Zhu Q, Sun J, Wang Y, et al. Tuning the carrier scattering mechanism to effectively improve the thermoelectric properties. *Energy Environ Sci.* 2017;10: 799–807. doi:10.1039/C7EE00098G
25. Gallicchio L, Fowler BA, Madden EF. Arsenic, antimony, and bismuth. In: Bingham E, Cohrssen B, Powell CH, editors. *Patty's Toxicology*. Hoboken, NJ, USA: John Wiley & Sons, Inc.; 2001. doi:10.1002/0471435139.tox036
26. Greenbank JC, Argent BB. Vapour pressure of magnesium, zinc and cadmium. *Trans Faraday Soc.* 1965;61: 655. doi:10.1039/tf9656100655
27. Imasato K, Wood M, Anand S, Kuo JJ, Snyder GJ. Understanding the high thermoelectric performance of Mg_3Sb_2 - Mg_3Bi_2 alloys. *Adv Energy Sustain Res.* 2022;3: 2100208. doi:10.1002/aesr.202100208
28. Liu X, Xi L, Qiu W, Yang J, Zhu T, Zhao X, et al. Significant roles of intrinsic point defects in Mg_2X ($\text{X} = \text{Si, Ge, Sn}$) thermoelectric materials. *Adv Electron Mater.* 2016;2. doi:10.1002/aelm.201500284
29. Wood M, Kuo JJ, Imasato K, Snyder GJ. Improvement of Low-Temperature zT in a Mg_3Sb_2 - Mg_3Bi_2 Solid Solution via Mg-Vapor Annealing. *Adv Mater.* 2019;31: e1902337. doi:10.1002/adma.201902337
30. Jørgensen LR, Zhang J, Zeuthen CB, Iversen BB. Thermal stability of $\text{Mg}_3\text{Sb}_{1.475}\text{Bi}_{0.475}\text{Te}_{0.05}$ high performance n-type thermoelectric investigated through powder X-ray diffraction and pair distribution function analysis. *J Mater Chem A.* 2018;6: 17171–17176. doi:10.1039/C8TA06544F
31. Song L, Zhang J, Iversen BB. Thermal stability of p-type Ag-doped Mg_3Sb_2 thermoelectric materials investigated by powder X-ray diffraction. *Phys Chem Chem Phys.* 2019;21: 4295–4305. doi:10.1039/c8cp07648k

32. Liu Z, Gao W, Oshima H, Nagase K, Lee C-H, Mori T. Maximizing the performance of n-type Mg₃Bi₂ based materials for room-temperature power generation and thermoelectric cooling. *Nat Commun.* 2022;13: 1120. doi:10.1038/s41467-022-28798-4
33. Webelements. In: Webelements [Internet]. [cited 16 Jul 2024]. Available: https://winter.group.shef.ac.uk/webelements/antimony/atom_sizes.html
34. Zeier WG. New tricks for optimizing thermoelectric materials. *Current Opinion in Green and Sustainable Chemistry.* 2017;4: 23–28. doi:10.1016/j.cogsc.2017.02.003
35. Peng W, Petretto G, Rignanese G-M, Hautier G, Zevalkink A. An unlikely route to low lattice thermal conductivity: small atoms in a simple layered structure. *Joule.* 2018;2: 1879–1893. doi:10.1016/j.joule.2018.06.014
36. Hu L, Zhu T, Liu X, Zhao X. Point defect engineering of high-performance bismuth-telluride-based thermoelectric materials. *Adv Funct Mater.* 2014;24: 5211–5218. doi:10.1002/adfm.201400474

Chapter 3: Supporting Information

SEM/EDS Analysis

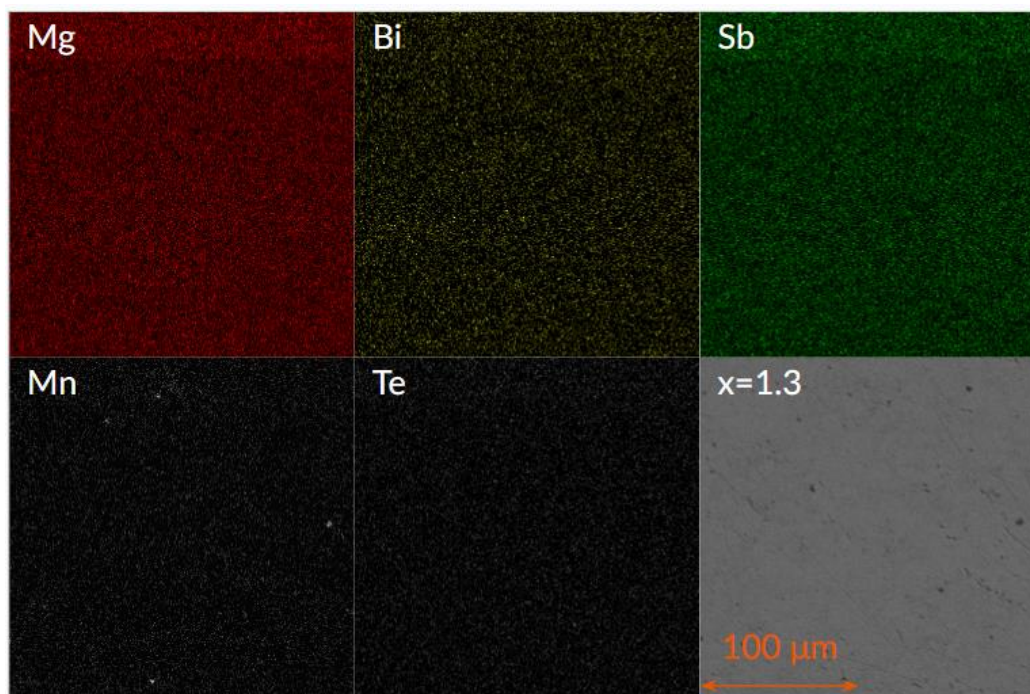


Figure S3.1. SEM/EDS analysis of the SPS $\text{Mg}_{3.27}\text{Mn}_{0.03}\text{Bi}_{1.3}\text{Sb}_{0.69}\text{Te}_{0.01}$ sample

Table S3.1. Atomic percent analysis of $\text{Mg}_{3.27}\text{Mn}_{0.03}\text{Bi}_{1.3}\text{Sb}_{0.69}\text{Te}_{0.01}$ sample

	Theoretical	Experimental
Mg	61.7	60.9(7)
Bi	24.5	24.1(2)
Sb	13.0	13.7(9)
Mn	0.6	0.6(3)
Te	0.2	0.4(9)

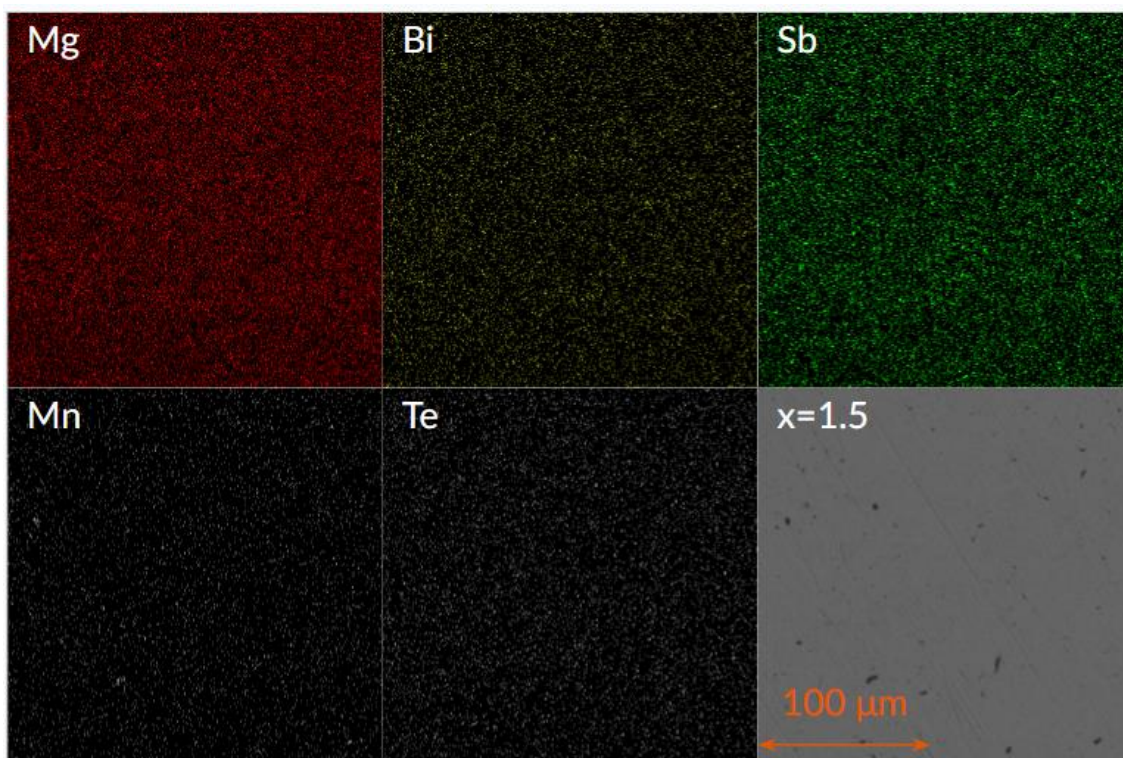


Figure S3.2. SEM/EDS analysis of the SPS Mg_{3.27}Mn_{0.03}Bi_{1.5}Sb_{0.49}Te_{0.01} sample

Table S3.2. Atomic percent analysis of Mg_{3.27}Mn_{0.03}Bi_{1.5}Sb_{0.49}Te_{0.01} sample

	Theoretical	Experimental
Mg	61.7	60.6(8)
Bi	28.3	29.5(2)
Sb	9.2	9.2(0)
Mn	0.6	0.4(3)
Te	0.2	0.1(7)

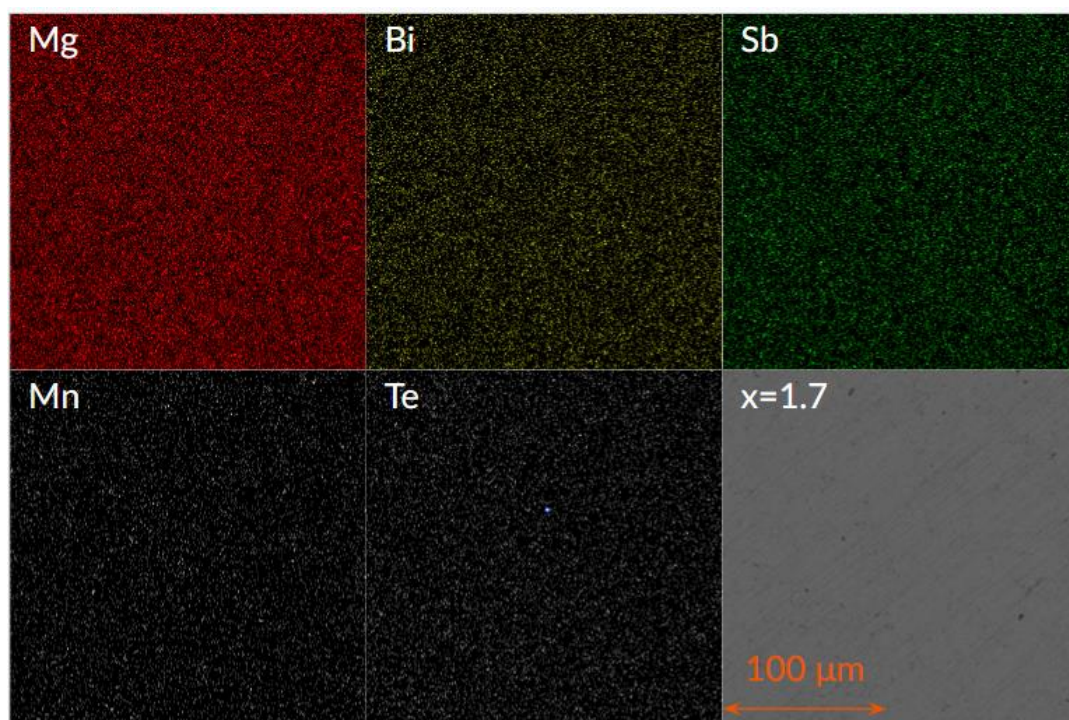


Figure S3.3. SEM/EDS analysis of the SPS $\text{Mg}_{3.27}\text{Mn}_{0.03}\text{Bi}_{1.7}\text{Sb}_{0.29}\text{Te}_{0.01}$ sample

Table S3.3. Atomic percent analysis of $\text{Mg}_{3.27}\text{Mn}_{0.03}\text{Bi}_{1.7}\text{Sb}_{0.29}\text{Te}_{0.01}$ sample

	Theoretical	Experimental
Mg	61.7	60.3(6)
Bi	32.1	32.8(4)
Sb	5.5	6.0(9)
Mn	0.6	0.4(7)
Te	0.2	0.2(4)

Chapter 4: Thermoelectric Properties of n-type Ni-doped and p-type

Mg₃Sb_{2-x}Bi_x Phases

Introduction

In this chapter, we explored the *n*-type Ni-doped samples with the goal of increasing the performance just above the room temperatures (below 100°C). We also synthesized *p*-type Mg₃(Bi,Sb)₂ by reducing the amount of extra Mg while maintaining the phase purity. Annealing after SPS were also carried out to enhance the sample purity as in the *n*-type samples [1].

Experimental

Starting elements Mg (powder, 99 wt.%, Sigma-Aldrich), Bi (99.999 wt.%, Alfa Aesar), Sb (powder, 99.999 wt.%, 5N Plus), Te (99.999 wt.%, Alfa Aesar), and Mn (powder, 99.99 wt.%, Alfa Aesar) and Ni (powder, 99.99 wt.%, Alfa Aesar) were weighed according to the Mg_{3.27}Mn_{0.03}Ni_{0.01}Bi_{1.5}Sb_{0.49}Te_{0.01} and Mg_{3.29}Ni_{0.01}Bi_{1.5}Sb_{0.49}Te_{0.01} composition for *n*-type. For *p*-type, Mg_{3.15}Bi₁Sb₁ and Mg_{3.15}Bi_{1.5}Sb_{0.5} were prepared.

The elements were loaded into a stainless-steel ball-milling jar inside a glove box in the argon atmosphere with oxygen levels below 0.1 ppm. The ball to sample weight ratio was 20:1. The jar was capped with an air-tight lid inside the glove box. The samples were then ball milled for 1 hour at 400 rpm using the planetary ball mill machine (Fritsch PULVERISETTE 6). The resulting powder was loaded into a 12.7mm graphite die inside the glovebox and sintered using spark plasma sintering (SPS, Dr. Sinter SPS 211) at 873K under a pressure of approximately 50 MPa for 5 minutes, and then annealed at 473K for 10 more minutes.

The sample purity was analyzed on the powder X-ray diffractometer (PANalytical X'Pert, CuK α 1, X'Celerator detector). The microstructure and composition were analyzed on

a scanning electron microscope (TESCAN VEGA) equipped with an energy dispersive spectrometer (EDS).

The Seebeck coefficient and electrical resistivity were measured simultaneously on a ZEM-3 system (ULVAC-RIKO, Japan) in a helium atmosphere at 0.01 MPa. Thermal diffusivity was measured on disc-shaped samples under argon flow conditions using laser flash analysis (Netzsch LFA-457). The thermal conductivity was calculated from $\kappa = D \cdot c_p \cdot \rho$, where D , c_p , and ρ are the thermal diffusivity, specific heat capacity, and density, respectively [2].

Results and Discussion for n-type Ni doped

PXRD Results

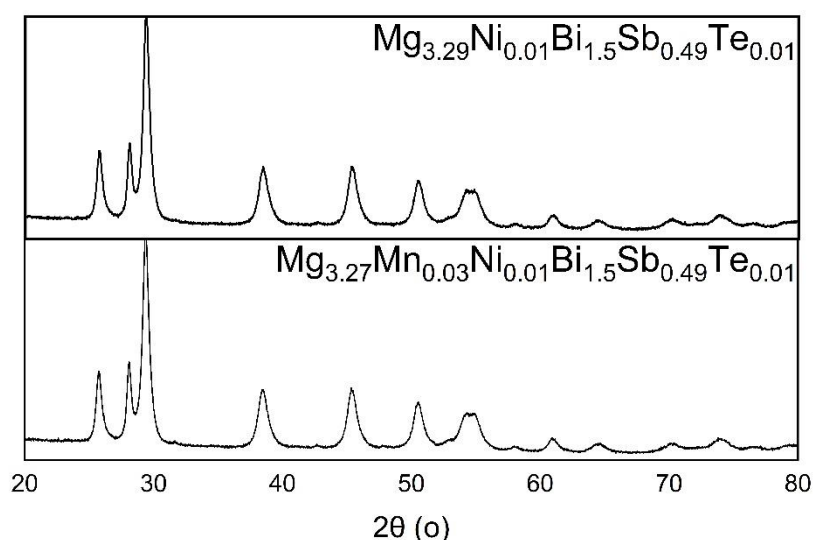


Figure 4.1. XRD patterns of $\text{Mg}_{3.29}\text{Ni}_{0.01}\text{Bi}_{1.5}\text{Sb}_{0.49}\text{Te}_{0.01}$ and $\text{Mg}_{3.27}\text{Mn}_{0.03}\text{Ni}_{0.01}\text{Bi}_{1.5}\text{Sb}_{0.49}\text{Te}_{0.01}$ after SPS

The first sample involves replacing Mn with Ni on the Mg site. The second sample uses Ni in addition to the Mn dopant. Using the same procedures as in Chapter 3, both samples were prepared phase pure, indicating successful synthesis as shown in Figure 4.1.

Electrical and Thermal Properties

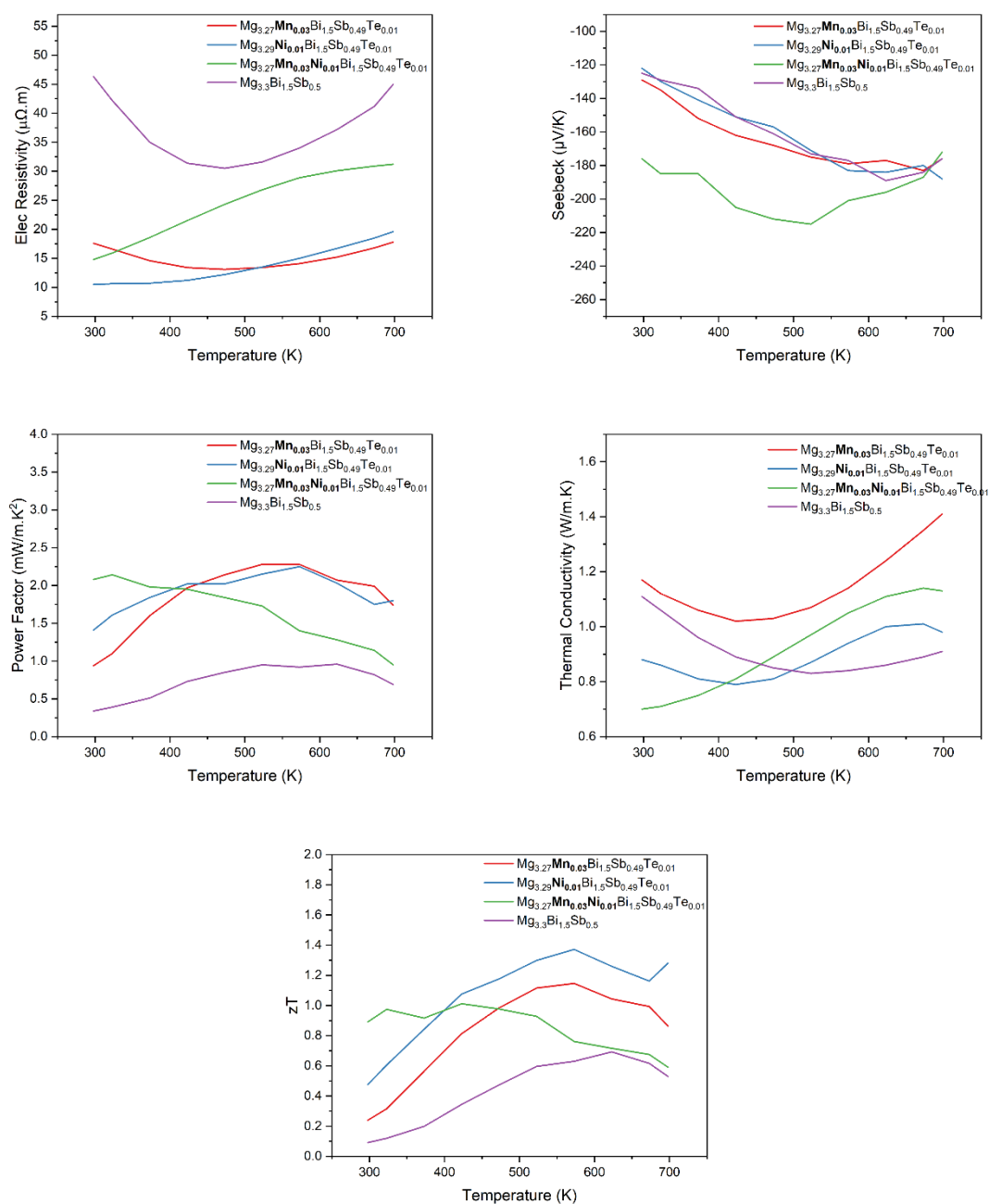


Figure 4.2. Electrical and Thermal Properties of $\text{Mg}_{3.29}\text{Ni}_{0.01}\text{Bi}_{1.5}\text{Sb}_{0.49}\text{Te}_{0.01}$ and $\text{Mg}_{3.27}\text{Mn}_{0.03}\text{Ni}_{0.01}\text{Bi}_{1.5}\text{Sb}_{0.49}\text{Te}_{0.01}$ in comparison with $\text{Mg}_{3.27}\text{Mn}_{0.03}\text{Bi}_{1.5}\text{Sb}_{0.49}\text{Te}_{0.01}$ and undoped $\text{Mg}_{3.3}\text{Bi}_{1.5}\text{Sb}_{0.5}$ sample

A comparative analysis of electrical and thermal properties was conducted between $\text{Mg}_{3.27}\text{Mn}_{0.03}\text{Bi}_{1.5}\text{Sb}_{0.49}\text{Te}_{0.01}$, undoped $\text{Mg}_{3.3}\text{Bi}_{1.5}\text{Sb}_{0.5}$, and Ni-doped variants (Figure 4.2). The

introduction of Ni resulted in an enhancement of the power factor within the lower temperature range, specifically below 100°C. This improvement is attributed to a low-temperature carrier scattering mechanism that simultaneously reduces thermal conductivity [3]. As a consequence, the $\text{Mg}_{3.29}\text{Ni}_{0.01}\text{Bi}_{1.5}\text{Sb}_{0.49}\text{Te}_{0.01}$ sample demonstrated better overall performance across the entire temperature range when compared to the other compositions. Notably, the $\text{Mg}_{3.27}\text{Mn}_{0.03}\text{Ni}_{0.01}\text{Bi}_{1.5}\text{Sb}_{0.49}\text{Te}_{0.01}$ sample exhibited a particularly pronounced performance boost at lower temperatures, with a zT increasing from 0.25 to 0.9 at room temperature, highlighting the effectiveness of the Ni doping strategy in this temperature range. These findings suggest the potential of Ni doping as a promising approach to optimize the thermoelectric properties of these materials for low-temperature range.

Results and Discussion for p-type $\text{Mg}_3(\text{Bi,Sb})_2$

PXRD Results

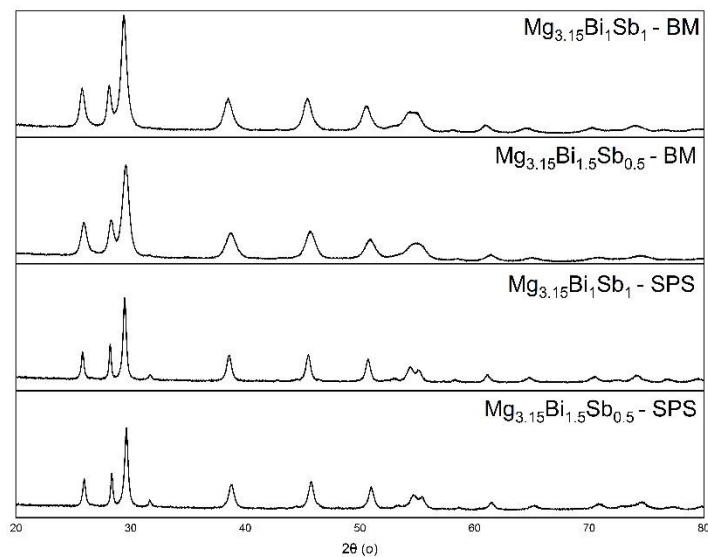


Figure 4.3. XRD patterns of $\text{Mg}_{3.15}\text{Bi}_1\text{Sb}_1$ and $\text{Mg}_{3.15}\text{Bi}_{1.5}\text{Sb}_{0.5}$ after ball mill (BM) and SPS

As in the previous chapter, excess Mg was important to achieve n-type conductivity. To create p-type materials, the Mg content was reduced from 3.3 to 3.15. The additional 0.15 atomic units of Mg above the stoichiometric amount were needed to maintain phase purity during synthesis. PXRD analysis revealed phase-pure $\text{Mg}_{3.15}\text{Bi}_1\text{Sb}_1$ and $\text{Mg}_{3.15}\text{Bi}_{1.5}\text{Sb}_{0.5}$ samples after ball milling (Figure 4.3). However, after SPS approximately 2-4 at.% percent of Bi impurities were detected (Figure 4.3). This impurity formation may be attributed to insufficient Mg amount.

Electrical and Thermal Properties

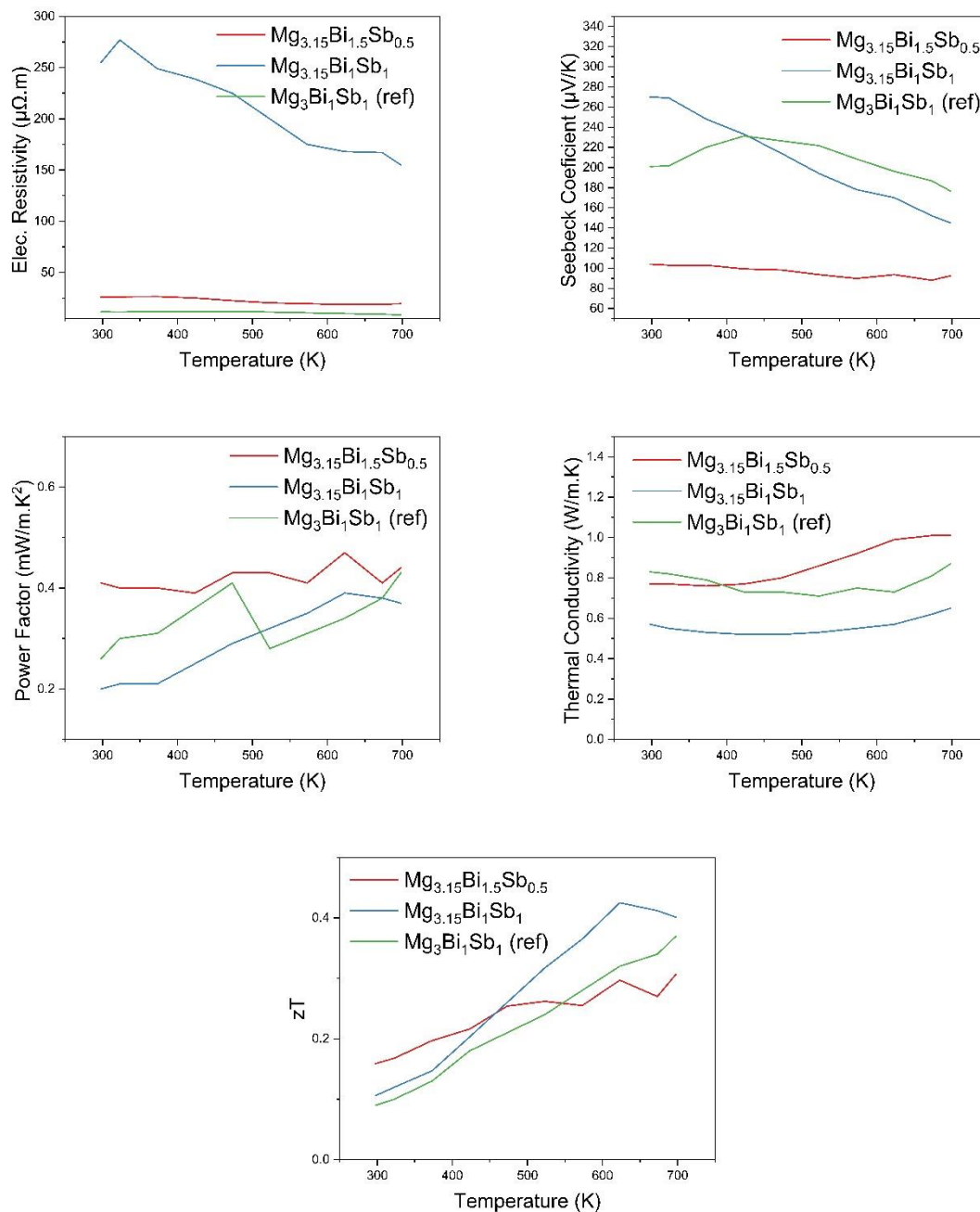


Figure 4.4. Electrical and Thermal Properties of $\text{Mg}_{3.15}\text{Bi}_1\text{Sb}_1$ and $\text{Mg}_{3.15}\text{Bi}_{1.5}\text{Sb}_{0.5}$ samples in comparison to the reference $\text{Mg}_3\text{Bi}_1\text{Sb}_1$ sample [4]

In general, both $\text{Mg}_{3.15}\text{Bi}_1\text{Sb}_1$ and $\text{Mg}_{3.15}\text{Bi}_{1.5}\text{Sb}_{0.5}$ samples exhibit properties similar to the reference sample (Figure 4.4) [4]. The $\text{Mg}_{3.15}\text{Bi}_{1.5}\text{Sb}_{0.5}$ sample displays a higher power

factor but lower thermal conductivity compared to the $\text{Mg}_{3.15}\text{Bi}_1\text{Sb}_1$ sample. The maximum zT value of approximately 0.4 is achieved for the $\text{Mg}_{3.15}\text{Bi}_1\text{Sb}_1$ sample at 625 K.

References

1. Wood M, Kuo JJ, Imasato K, Snyder GJ. Improvement of Low-Temperature zT in a Mg_3Sb_2 - Mg_3Bi_2 Solid Solution via Mg-Vapor Annealing. *Adv Mater.* 2019;31: e1902337. doi:10.1002/adma.201902337
2. Chen X, Wu H, Cui J, Xiao Y, Zhang Y, He J, et al. Extraordinary thermoelectric performance in n-type manganese doped Mg_3Sb_2 Zintl: High band degeneracy, tuned carrier scattering mechanism and hierarchical microstructure. *Nano Energy.* 2018;52: 246–255. doi:10.1016/j.nanoen.2018.07.059
3. Li Z, Sun C, Li X, Ye X, Yang K, Nie X, Zhao W, Zhang Q. Realizing Excellent Structural and Thermoelectric Performance in Mg_3Sb_2 -Based Alloys by Manipulating Mg Intrinsic Migration Kinetics with Interstitial Ni Doping. *ACS Appl Mater Interfaces.* 2023 May 17;15(19):23447-23456. doi: 10.1021/acsami.3c02351
4. Ponnambalam, V., Morelli, D.T. On the Thermoelectric Properties of Zintl Compounds $\text{Mg}_3\text{Bi}_{2-x}\text{Pn}_x$ (Pn = P and Sb). *J. Electron. Mater.* **42**, 1307–1312 (2013). <https://doi.org/10.1007/s11664-012-2417-7>

Conclusions and Future Work

In conclusion, both n-type and p-type $\text{Mg}_{3+y}\text{Bi}_x\text{Sb}_{2-x}$ have been successfully synthesized. Their properties are comparable to reference data. For n-type, it is important to note the role of extra Mg, proper ball milling time, and thermal annealing to produce $\text{Mg}_{3.27}\text{Mn}_{0.03}\text{Bi}_x\text{Sb}_{1.99-x}\text{Te}_{0.01}$ samples with suitable thermoelectric properties. The peak zT value of 1.55 for $x = 1.3$ at 623 K suggests that $\text{Mg}_{3.27}\text{Mn}_{0.03}\text{Bi}_x\text{Sb}_{1.99-x}\text{Te}_{0.01}$ samples can be suitable for low to mid-range temperature applications. If the thermal stability of the $\text{Mg}_{3.27}\text{Mn}_{0.03}\text{Bi}_x\text{Sb}_{1.99-x}\text{Te}_{0.01}$ materials could be improved, their low cost, environmental friendliness, and comparable performance could position them as a potential replacement for Bi_2Te_3 .

Ni doping was also explored along with Mn, and the results suggest a slight increase in zT for $\text{Mg}_{3.29}\text{Ni}_{0.01}\text{Bi}_x\text{Sb}_{1.99-x}\text{Te}_{0.01}$ compared to $\text{Mg}_{3.27}\text{Mn}_{0.03}\text{Bi}_x\text{Sb}_{1.99-x}\text{Te}_{0.01}$. This is a very promising approach, especially to enhance the properties at the low temperature range (below 100°C).

By reducing the extra Mg, p-type was synthesized and showed comparable properties to the reference data. Several approaches, including doping and optimizing the annealing temperature, were carried out to enhance the properties but were unsuccessful.

Future work should focus on improving thermal stability of the samples, especially those with a high ratio of Bi. Additionally, enhancing the p-type properties is crucial so that thermoelectric couples can be fabricated and tested in practical applications.